2022

A COUPLED VISCOPLASTIC-DAMAGE CONSTITUTIVE MODEL FOR SEMICRYSTALLINE POLYMERS

Jeffrey Wiersma
Michigan Technological University, jjwiersm@mtu.edu

A COUPLED VISCOPLASTIC-DAMAGE CONSTITUTIVE MODEL FOR SEMICRYSTALLINE POLYMERS

By

Jeffrey Wiersma

A DISSERTATION

Submitted in partial fulfillment of the requirements for the degree of

DOCTOR OF PHILOSOPHY

In Mechanical Engineering-Engineering Mechanics

MICHIGAN TECHNOLOGICAL UNIVERSITY

2022

This dissertation has been approved in partial fulfillment of the requirements for the Degree of DOCTOR OF PHILOSOPHY in Mechanical Engineering-Engineering Mechanics.

Department of Mechanical Engineering-Engineering Mechanics

Dissertation Advisor:	*Dr. Trisha Sain*
Committee Member:	*Dr. Gregory Odegard*
Committee Member:	*Dr. Ibrahim Miskioglu*
Committee Member:	*Dr. Qingli Dai*
Department Chair:	*Dr. Jason Blough*

Dedication

To my family,

This work would not be possible without your love and support.

To my daughters,

Thank you for your understanding and willingness to let dad spend hours at his desk during the evenings and weekends.

Table of Contents

List of Figures vii

List of Tables x

Acknowledgements xi

List of Abbreviations xii

Abstract xvi

1 Introduction 1

1.1 Background and literature review 1

1.1.1 Large deformation mechanism 1

1.1.2 Constitutive theories 2

1.1.3 Damage process for semicrystalline materials 5

1.1.4 Damage modeling for semicrystalline materials 7

1.2 Research objective 8

1.3 Methodology 9

1.3.1 Elastic-viscoplastic constitutive model 9

1.3.2 Continuum scale damage model 10

2 A coupled viscoplastic-damage constitutive model for semicrystalline polymers 12

2.1 Introduction 12

2.2 Experimental testing of polypropylene homopolymer 14

2.2.1 Sample preparation 14

2.2.2 Tensile testing 15
2.2.3 Simple compression testing 17
2.2.4 Notched cylindrical tensile bar testing 18
2.2.5 Tensile testing of a thin plate with circular hole 21
2.2.6 Three-point bend testing of a notched beam 23
2.3 Constitutive model for semicrystalline polymer 26
2.3.1 Kinematics of deformation 26
2.3.2 Free energy 30
2.3.3 Equation for stress and back stress 32
2.3.4 Flow rule 34
2.3.5 Evolution of the internal plastic variables, $S1$ and ϕ 36
2.3.6 Damage model for semicrystalline polymers 38
2.4 Estimation of the material parameters for polypropylene 43
2.5 Numerical simulations and comparison with experiments 55
2.5.1 Uniaxial tension simulation for a 3D dog-bone geometry 56
2.5.2 Uniaxial compression simulation of a 3D cylinder 60
2.5.3 Tensile simulation of a thin plate with circular hole at the center 63
2.5.4 Three-point bending of a notched beam 66
2.6 Concluding remarks 69
3 Future recommendations 71
4 References 74
Appendix 83

A.1 Numerical implementation of the explicit stress update 83

List of Figures

2.1. True stress versus logarithmic strain in tension for isotactic polypropylene homopolymer for three different strain rates. 16

2.2. True stress versus logarithmic strain in compression for isotactic polypropylene homopolymer for three different strain rates. 17

2.3. Geometry and dimensions of the notched cylindrical tensile bars. 19

2.4. Average fracture strain, ε_c versus stress triaxiality, η 20

2.5. Plate with a circular hole geometry. 21

2.6. Experimental force-displacement curves for the thin plate with circular hole. ... 22

2.7. DIC for strain (ε_{22}) for the thin plate with circular hole. 23

2.8. Notched three-point bend beam geometry. 24

2.9. Experimental force-displacement curves for the notched beam in three-point bending. 25

2.10. DIC for strain (ε_{11}) for the notched beam in three-point bending. 26

2.11. Tensile yield stress versus input logarithmic strain rate at room temperature (296 K). 47

2.12. Compressive yield stress versus input logarithmic strain rate at room temperature (296 K). 47

2.13. Comparison between the calibrated constitutive model and the experimental stress-strain response of the polypropylene in tension. 49

2.14. Comparison between the calibrated constitutive model and the experimental stress-strain response of the polypropylene in compression. 50

2.15. Stress independent constant $(dR/R)_c$ as a function of stress triaxiality, η for different strain rates. 54

2.16. β as a function of input strain rate, $\dot{\varepsilon}$. 55

2.17. (a) Specimen geometry and boundary conditions. (b) 8-noded hexahedron mesh using C3D8R elements. 57

2.18. (a) Comparison between the model prediction and experimental load-displacement curve. (b) Maximum principal stress contour corresponding to load point (1). (c) Equivalent plastic shear strain contour corresponding to load point (1). (d) Damage variable, *d*, corresponding to point (2) right after complete fracture. (e) Principal logarithmic strain at point (3) as the neck propagates for the $10^{-3}\ s^{-1}$ strain rate along the gauge section. 59

2.19. (a) Experimental specimen geometry. (b) 1/4 model finite element mesh discretization using ABAQUS-C3D8R elements..... 60

2.20. (a) Comparison between the experiments and numerically predicted load-displacement curve. (b) Maximum principal stress plot corresponding to load point (1). (c) Equivalent plastic shear strain corresponding to load point (1). (d) Maximum principal logarithmic strain corresponding to load point (1). 62

2.21. (a) Specimen geometry for the plate with a hole simulation. (b) Finite element mesh discretization using ABAQUS-C3D8R elements. 63

2.22. Comparison between the experiments and numerically predicted load-displacement curve. (b) Maximum principal stress plot corresponding to load point (1). (c) Equivalent plastic shear strain corresponding to load point (1). (d) Damage variable, *d*, corresponding to point (2) right after complete fracture. (e) Maximum principal strain ε_1 corresponding to point (1). (f) DIC strain contour for (ε_{22}). 65

2.23. (a) Simulation specimen for the three-point bend geometry. (b) Finite element mesh discretization using ABAQUS-C3D8R elements. 66

2.24. Comparison between the experiments and numerically predicted load-displacement curve. (b) Maximum principal stress plot corresponding to load point (1). (c) Equivalent plastic shear strain corresponding to load point (1). (d) Damage variable, *d*, corresponding to point (2) right after complete fracture. (e) Maximum principal strain ε_1 corresponding to point (1). (f) DIC strain contour for (ε_{22}). 68

List of Tables

2.1 Material parameters for polypropylene homopolymer 51

Acknowledgements

I would like to express my sincere gratitude to my advisor, Dr. Trisha Sain, who has supported me throughout this research project. Your patience and willingness to advise a distance student was instrumental to the success of this research.

I would like to thank my dissertation advisory committee members, Dr. Gregory Odegard, Dr. Ibrahim Miskioglu, Dr. Qingli Dai, for providing your knowledge and expertise on the subject manner.

I would like to thank MillerKnoll Inc., for funding the entirety of this work.

List of Abbreviations

η	Triaxiality ratio
σ_m	Mean normal stress
$\bar{p}$	Mean normal pressure
σ_{eq}	von Mises equivalent stress
ε_c^P	Experimental critical failure strain for notched tensile bar
ε_{eq}^p	Equivalent plastic strain
ε_i^p	Critical equivalent plastic strain for the onset of cavitation damage
D_0	Minimum section diameter for the notched tensile bar
D_c	Measured section diameter at fracture for the notched tensile bar
$\boldsymbol{F}$	Deformation gradient
$\boldsymbol{F}^e$	Elastic deformation gradient
$\boldsymbol{F}^p$	Plastic deformation gradient
$\boldsymbol{L}$	Velocity gradient
$\boldsymbol{C}^e$	Right elastic Cauchy-Green tensor

$\boldsymbol{B}^p$	Left plastic Cauchy-Green tensor
$\boldsymbol{B}_0^p$	Deviatoric component of the left plastic Cauchy-Green tensor
$\boldsymbol{D}^p$	Plastic stretching rate tensor
$\boldsymbol{E}^e$	Elastic Green strain tensor
$\boldsymbol{E}_0^e$	Deviatoric component of the elastic Green strain tensor
ψ^e	Elastic free energy
ψ_e^D	Damaged elastic free energy
ψ^p	Plastic free energy
λ^p	Effective distortional plastic stretch
λ_L	Network locking stretch
G	Shear modulus
K	Bulk modulus
μ_R	Rubbery modulus
μ	Back stress modulus
$\boldsymbol{S}^e$	Second Piola-Kirchoff stress tensor
$\boldsymbol{S}^{eD}$	Damaged second Piola-Kirchoff stress tensor

$\boldsymbol{S}_D$	Damaged stress tensor
$\boldsymbol{S}_0^e$	Deviatoric component of the second Piola-Kirchoff stress tensor
$(\boldsymbol{S}_0^e)_{eff}$	Effective second Piola-Kirchoff stress tensor
$\boldsymbol{S}_{back}$	Back stress tensor
$\dot{\gamma^p}$	Equivalent plastic shear strain rate
$\dot{\gamma_0}$	Reference shear strain rate parameter
Q	Activation energy
V	Activation volume
k_B	Boltzmann's constant
ϑ	Reference temperature
m	Strain rate sensitivity parameter
$\bar{\tau}$	Equivalent shear stress
α_p	Pressure sensitivity material parameter
τ_e	Net shear stress for thermally activated flow
${\tau_e}^D$	Damaged net shear stress for thermally activated flow
S_1	Internal plastic variable: Flow resistance

S_1^*	Internal plastic variable: Flow resistance saturation value
h_1	Material parameter for S_1 controlling the yield-peak slope
ϕ	Internal plastic variable: Order parameter
ϕ^*	Internal plastic variable: Order parameter saturation value
g	Material parameter for ϕ controlling the yield peak width
β	Rice-Tracey parameter for the interaction of neighboring voids.
d	Scalar damage parameter
d_c	Critical scalar damager parameter for fibrillation and element deletion

Abstract

The ease of processing, recyclability, and ideal cost to weight ratio makes the semi-crystalline polymers attractive in the aerospace, automotive, and defense industries. Use of semicrystalline polymers for engineering design requires a thorough understanding of their response to mechanical deformation, rate of loading, temperature, and failure mechanisms. However, there lacks a generally agreed upon constitutive model to capture the large deformation elastic-viscoplastic response of semicrystalline polymers while incorporating the strain-rate dependence and damage behavior. To address this aspect, the objective of this dissertation is to develop an elastic-viscoplastic constitutive model to predict the rate dependent, large deformation response of semicrystalline polymers under tension and compression. In addition, a continuum scale damage model coupled with viscoplasticity is adopted to incorporate cavitation induced damage growth, coalescence, and fibrillation in the material. To validate the proposed model, uniaxial compression and tension experiments are conducted on isotactic polypropylene homopolymer within strain rates of 10^{-3} s^{-1} to 10^{-1} s^{-1}. The constitutive model is implemented in a finite element program ABAQUS/Explicit (ABAQUS 2017) by writing a user material subroutine (VUMAT). With the model parameters properly calibrated, the present study shows that the proposed constitutive model is able to predict the macroscopic rate dependent load-displacement curves, as well as the fracture responses for various standard geometries.

1 Introduction

1.1 Background and literature review

Semicrystalline polymers are comprised of both amorphous and crystalline regions. The crystalline phases are characterized by three-dimensional regions associated with the ordered stacking of adjacent chains into lamellae. This phase is responsible for the polymer's rigidity, yet it also makes the polymer less ductile. The amorphous regions are made up of randomly coiled and entangled chains and offer the polymer its ductility. A semicrystalline polymer can therefore be viewed as composite of rigid crystallites suspended in an amorphous phase [45]. This arrangement offers this two-phase polymer the advantage of the strength from the crystalline phase while leveraging the ductility of the amorphous counterpart.

1.1.1 Large deformation mechanism

The large deformation mechanism for semicrystalline polymers are well understood [29]. In general, the process of deformation until failure can be broken into a few phases. In the

first phase, the viscoelastic deformation is considered as caused by the elongation of the amorphous tie chains and a reversible swelling of the lamellae [10]. In the second phase the polymer begins to yield when an increased load on the molecular chains, primarily in the crystalline phase, reaches a required threshold of thermodynamic potential and slippage of the chains begins to ensue [17]. Following this stage, the larger crystalline domains begin to split, and the entangled, amorphous chains start to release, leading to a significant macro level softening for some materials [10]. The final phase is characterized by the re-alignment of both the amorphous and crystalline regions resulting in continuous entropic hardening that leads to fibrillation and molecular chain scission.

1.1.2 Constitutive theories

There are various forms of constitutive theories that have been developed to represent the deformation behavior of the semicrystalline polymers. As reported in [43], two major types of constitutive models are outlined as micromechanical models and phenomenological models. Micromechanical models predict material response by simulating interactions on the atomic, molecular, or crystalline levels, whereas phenomenological or "macroscopic" models rely on observations of representative volumes of material. A comprehensive review of constitutive descriptions of semicrystalline polymers for both micromechanics and macroscale modeling has been presented by [27].

At the micro level, the material is typically modeled by considering the two structural phases – crystalline and amorphous [45]. It is known that semicrystalline polymers have highly anisotropic microstructures [17], yet generally exhibit an isotropic response on the macro scale, under ideal molding conditions [27]. Typically, an anisotropic arrangement is assumed for the molecular chains and their rearrangement occurs via a thermally activated mechanism. Drozdov and coworkers have done considerable work on the micromechanics of both amorphous and semi-crystalline polymers [16, 17, 18, 19, 20], particularly on the kinetics of chain rearrangement. They are able to show good agreement between model prediction and experimental observation in the small strain regime [17, 19, 20,] for two of the commonly used polymers, polyethylene, and polypropylene. However, micro-scale modeling is often accompanied by considerable difficulty to correlate the complex microstructure with the constitutive response for semicrystalline polymers.

At the macro level, it is often assumed that the deformation response can be modeled as an isotropic phase where the crystalline and amorphous regions are homogenized. The early work of Haward-Thackray, [26] proposed a one-dimensional constitutive theory for glassy polymers; incorporating both yielding and strain hardening phenomena. This approach was later followed by many of the three-dimensional models proposed to describe the constitutive behavior for glassy polymers [7, 11, 59] and recently for high density polyethylene (HDPE) by [8]. Hughes, [28] looked at the mechanical response of ultra-high molecular weight polyethylene (UHMWPE) using a classical isotropic, rate-independent plasticity model following a Mises yield criterion. However, this model was not able to provide reliable predictions of the non-linear behavior experienced during large

deformations. Early viscoelastic models included the work by Popelar et. al. [44], who proposed a phenomenological approach using a nonlinear viscoelastic model for semicrystalline polymers based on the original work by Shapery [50]. Later on, his research progressed to include viscoplasticity for polyamide 66 [33] and for HDPE [25], where an over-stress dependent viscosity parameter and nonlinear equilibrium stress evolution were used as state variables to model the viscoplastic behavior.

It is noted that there are few macro scale models available in literature that offer a comprehensive three-dimensional characterization that include the polymers' thermo-mechanical response, as well as the strain rate and temperature dependent, yielding response, and additionally the post-yield softening and hardening behavior [3, 4, 5, 37, 52]. Although these works focused on the theoretical modeling of amorphous polymers, their ability to capture the salient features of the macroscale response which are very similar to the response observed in many semicrystalline polymers; widen their domain of applications. It is to be noted that specifically the rate and temperature dependent yield stress, as well as the post yield softening and hardening behavior are quite similar in the amorphous and semicrystalline polymers.

1.1.3 Damage process for semicrystalline materials

The fracture of semicrystalline polymers can occur in either a brittle or ductile manner, or in various combinations of the two [63]. The primary damage mechanisms are caused by cavitation and crazing when the material is subjected to tensile loading. Cavitation is defined as the formation of cavities or voids in the bulk of the solid polymer, occurring primarily around the yield-point. Cavitation or crazing only occurs in the presence of hydrostatic stress states induced form tension and cannot occur in either compression or shear [42]. Cavities can range in size from a few nanometers to several micrometers. Larger cavities will tend to scatter light, which can often be seen on the macroscale as whitening of the material and clearly visible during tensile testing [40].

Although there is still debate on where void nucleation occurs, it is generally accepted that the voids begin to nucleate in the amorphous phase between two adjacent crystalline lamellae in the equatorial region of the spherulite when subjected to hydrostatic stress states [36]. Once a cavity begins to nucleate, it will tend to grow and coalesce with neighboring voids. Although cavitation often dominates the damage response, crazes may also generate from partial merging of voids where oriented microfibrils bridge the surfaces of neighboring voids. However, in contrast to cracks, crazes can transfer stress due the presence of microfibrils.

The general process of crazing is well understood for amorphous polymers below the glass transition temperature [2]. However, for semicrystalline polymers, crazing and cavitation can occur above and below the glass transition temperature [14]. Although there still exists much debate surrounding the governing factors that determine whether a semicrystalline polymer will craze, cavitate, or both, it is generally accepted that there exists a competition process to determine if a void or cavity will nucleate [40]. If the strength of the amorphous phase is lower than the stress of initiation of the plastic deformation of the crystals, then cavitation occurs, else plastic deformation of the crystals will ensue and cavitation will not occur [42]. The damage mechanism for semicrystalline polymers is complex and often depends on the crystallinity, crystalline structure, chain orientation, number of tie-chains in the inter-lamellar amorphous region, and additionally the testing environment. [36]. A cavitation can also turn in to a craze or a craze can turn into a cavitation. For semicrystalline polymers such as polyoxymethylene (POM), polypropylene (PP), and high density polyethylene (HDPE), cavitation is often the dominate damage mechanism, whereas, semicrystalline polymers like polyamide-6 (PA6) low density polyethylene (LDPE) cavitation may not occur [41].

Once the material nucleates a void in the amorphous region, micro-void coalescence will drive void damage growth, ultimately leading to a phase change of the polymorphic material from amorphous and crystalline to the aligned state culminating in fibrillation and molecular chain scission [40].

1.1.4 Damage modeling for semicrystalline materials

Semicrystalline polymers are inherently prone to damage, and over time, the formation of damages such as crazing and cavitation cause a degradation in mechanical properties, which eventually result in failure of the material. The focus of damage mechanics is on the evaluation of the damage process, where damage occurs due to irreversible changes in the microstructure during deformation (e.g., micro-void nucleation, coalescence, fibrillation, and chain scission). Damage behavior can be included in the constitutive equations for the mechanical behavior of thermoplastic polymers and there are several approaches found in the literature.

One approach is to introduce the effect of damage through a micromechanical approach [23], which was originally developed for porous metallic materials. The advantage of a micromechanics approach is that it provides a connection between the microstructure and mechanical behavior of the material, however it requires a thorough understanding of the involved degradation mechanisms found at the macromolecular scale [15]. The Gurson–Tvergaard–Needleman (GTN) model [23] is one of the most widely used models based on this theory. The GTN model, which is well known for modeling the ductile damage for metallic materials, was also extended to investigate thermoplastic polymers. Some examples for amorphous materials are [12, 22, 61, 62]. Laiarinandrasana and colleagues [34], developed a micromechanical approach that considered porosity, rate, and

temperature dependency for semicrystalline polyvinylidene flouride (PVDF), however this work focused exclusively on the development of crazes.

Another approach found in the literature is that of continuum damage mechanics (CDM) [35]. In contrast, CDM is based on the thermodynamics of irreversible processes where a scalar damage variable D is used to represent the material degradation at the macroscopic scale [13]. Balieu et. al. [9] modified this approach and extended it to semicrystalline polymers where an elastic-viscoplastic model for 20% glass filled polypropylene was developed that considered a pressure dependent yield surface coupled with damage to consider both rate and pressure dependency. Other examples for amorphous polymers include [32, 39, 46, 51, 54, 55, 56, 57]. Recently, [38] developed a gradient-damage theory for the deformation and failure of amorphous polymers, which depends on the damage variable and its gradient. Additionally, [30] developed a new thermodynamically consistent damage model based on the Eindhoven Glassy Polymer (EG) multimode model that considers the effect of plastic deformation and hydrostatic stress on damage evolution.

1.2 Research objective

The overall objective of this research is to develop a predictive model framework to capture the large deformation and damage response on a continuum level scale for semicrystalline polymers. The first task in this research is to develop continuum level constitutive model

that can be used to model the polymers response in tension and compression in the large strain regime. The second task in this research is to develop a continuum level model that effectively captures the damage response for various geometries and loading conditions.

1.3 Methodology

The research objectives outlined above are accomplished with the methodologies outlined in chapter two of this dissertation. Chapter 2 is in the form of an article that that has been submitted to the journal Mechanics of Materials (MOM) and is currently under review. First author Jeff Wiersma has contributed as a whole to writing the manuscript, generating all experimental and numerical results, and proposing the theory presented in the manuscript. Dr. Trisha Sain has supervised the entire works, edited the manuscript, and the responsible person for any future communication.

1.3.1 Elastic-viscoplastic constitutive model

The initial approach to this research was first to develop a working understanding of the micro and macromechanics response for semicrystalline polymers subjected to rate-dependent large deformation loads during tension and compression. Rate dependent

experiments were conducted for tension and compression for a commercial grade of isotactic polypropylene homopolymer. A comprehensive literature review was conducted to assess the current state of research for constitutive theories applied to amorphous and semicrystalline polymers for the continuum scale, in the large deformation regime. This effort led to and overall understanding of the current research state with respect to capturing the salient features of the macro level, rate dependent large deformation response for semicrystalline polymers, specifically isotactic polypropylene homopolymer, as well as the current limitations.

Following this effort, an elastic-viscoplastic constitutive theory was proposed to model the rate dependent, large deformation response for semicrystalline polymers under tension and compression. This model is outlined in chapter 2.

1.3.2 Continuum scale damage model

The next step to this research was to develop an understanding of the micro and macromechanics damage responses inherent in semicrystalline polymers subjected to rate dependent loading. Experiments were conducted on notched cylindrical tensile bars to determine the critical failure strain as a function of triaxiality ratio and strain rate. Additionally, various test geometries were tested at to capture their rated dependent

damage response. An extensive literature review was conducted, and a proposed Rice-Tracey continuum scale model coupled with viscoplasticity is presented in chapter 2.

2 A coupled viscoplastic-damage constitutive model for semicrystalline polymers

2.1 Introduction

Semicrystalline polymers are extensively used in various industries including aerospace, automotive, oil and gas platforms, as well as consumer products. As such, one of the most relevant subjects of polymer mechanics is the understanding of the deformation mechanisms and fracture responses of semi-crystalline polymers. Chapter one outlines the background and comprehensive literature review, as well as the research objective and methodology.

The purpose of this paper is to present an alternative approach (more aligned to describe the amorphous polymer) to modeling the rate dependent, large deformation response of semicrystalline, thermoplastic polymers. Instead of considering the individual amorphous and crystalline phases separately, a homogeneous large deformation theory within a thermodynamically consistent framework is used. Considering the previous work of [4] as a starting point for the thermodynamically consistent constitutive theory, a thermally activated flow rule is adopted to model the rate dependent yielding for a class of semicrystalline polypropylene. The polymer's post yield thermal softening, and hardening

phases experienced during large strain environments are additionally modeled with the specific choice of evolution equations. In addition, a continuum damage model coupled with viscoplastic deformation is proposed to incorporate cavitation induced damage in the semicrystalline polymers. It is important to note, that taking a homogenized constitutive approach for the two-phase polymer may be limiting in the sense that the evolution of the intermolecular resistances in the amorphous and crystalline phases are not considered independently. This may limit the model's applicability for the strain rate regime where micro mechanisms for each individual phases influence the local deformation. However, by adopting a homogenized approach, the present model avoids treating the inherently complex relationships between the intermolecular resistances and their subsequent evolutions in a large deformation setting. This further allows a reduction in model parameters, as well as a simplification to the cavitation induced damage model.

The proposed constitutive model is implemented in an FEM software (ABAQUS/Explicit) via a user-defined material subroutine (VUMAT) and validated by experiments conducted at different loading rates. Additional simulations are carried out for a thin plate with hole under tension, as well as for a notched three-point beam in bending. When suitably implemented and calibrated, the proposed model is able to reasonably well predict the macroscopic rate dependent, load-displacement curves for a variety of geometric specimens.

This paper is organized as follows. In section 2.2, experiments are described and analyzed for a grade of polypropylene. In section 2.3, the constitutive model and the damage model

is presented. In section 2.4, a detailed description is provided for the calibration of the material parameters for polypropylene using the experimental data. In section 2.5, the predictive capabilities of the constitutive model are verified with various test geometries. Finally, section 6 closes with some concluding remarks. Finally, section 2.6 closes with some concluding remarks.

2.2 Experimental testing of polypropylene homopolymer

2.2.1 Sample preparation

The isotactic polypropylene homopolymer investigated in this work was provided by Flint Hills Resources (P9G1Z-047) in pellet form. This polypropylene is identified as an isotactic homopolymer with a melt flow rate (MFR) of 0.43 g/10 min. The pellet form was then extruded by Mitsubishi Chemical to a plaque size of 1220 mm x 1220 mm x 25.4 mm. In order to ensure the most consistent physical properties for both tensile and compressive specimens, all samples were machined to specification by CNC fabrication. Samples are fabricated as-machined surfaces, without any additional polishing. All samples were annealed at room temperature for 48 hrs. at 23 deg. C. All testing was conducted at room temperature at 23 deg. C +/- 2 deg. C.

2.2.2 Tensile testing

Tensile samples are machined in the longitudinal direction to an ASTM D638-02 Type-1 specimen with a nominal dimension of 3.1 mm in thickness, 13 mm in width, and 57 mm in gauge section length. Testing is conducted using an MTS system with a 10 kN capacity load frame. Crosshead controlled tests are conducted on all tensile samples and a video extensometer system (MTS AVX Advantage Video System) is used to measure strain directly for the strain rates of 10^{-3} s^{-1}, 10^{-2} s^{-1}, and 10^{-1} s^{-1} respectively. Three specimens are tested for each input strain rate and Poisson's ratio is measured directly with the video extensometer system for the strain rate of 10^{-3} s^{-1}. The rate dependent stress-strain curves obtained from the tests are as shown in Fig. (2.1).

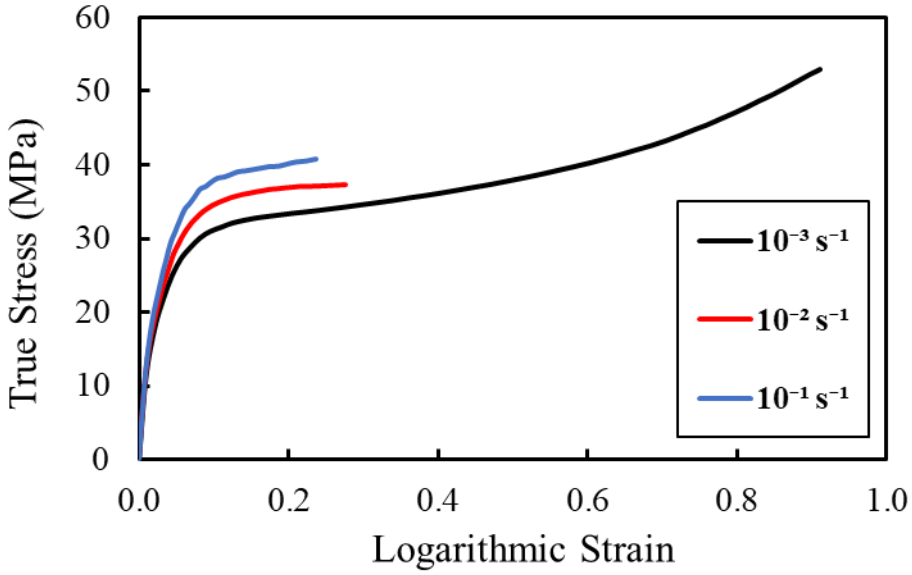

Figure 2.1. True stress versus logarithmic strain in tension for isotactic polypropylene homopolymer for three different strain rates.

For the 10^{-3} s^{-1} data as shown in Fig. 2.1, it should be noted that the test was stopped at a logarithmic strain of 0.93 mm/mm as the sample continued to stretch and did not fracture. It should also be noted that, for this extruded melt sample, it is possible to apply a very large stretch in excess of $\lambda = 8$ or even higher. Above the rate of 10^{-3} s^{-1}, samples were found to fracture in strain ranges of 0.2 to 0.4 mm/mm as shown in Fig. 2.1. Therefore, in tension, a post yield hardening phase is only observed when input strain rates of 10^{-3} s^{-1} or less are applied and the material shows substantial necking and ductility. Poisson's ratio was determined experimentally to be 0.36.

2.2.3 Simple compression testing

Compression samples are machined to a cylinder size of 9.80 mm in diameter and 9.85 mm in height. These specimens are compressed between polished steel platens lined with 1 mm thick Teflon sheets to ensure that friction does not affect the homogeneous deformations during large strains. Constant rate compression tests are performed using an MTS system for strain rates of 10^{-3} s^{-1}, 10^{-2} s^{-1}, and 10^{-1} s^{-1} respectively as per ASTM D695-15 specification. Testing is conducted using an MTS system with a 10,000 N capacity load frame since the servo-hydraulic machine will tend to generate very high applied forces to achieve the 10^{-1} s^{-1} applied true strain rate.

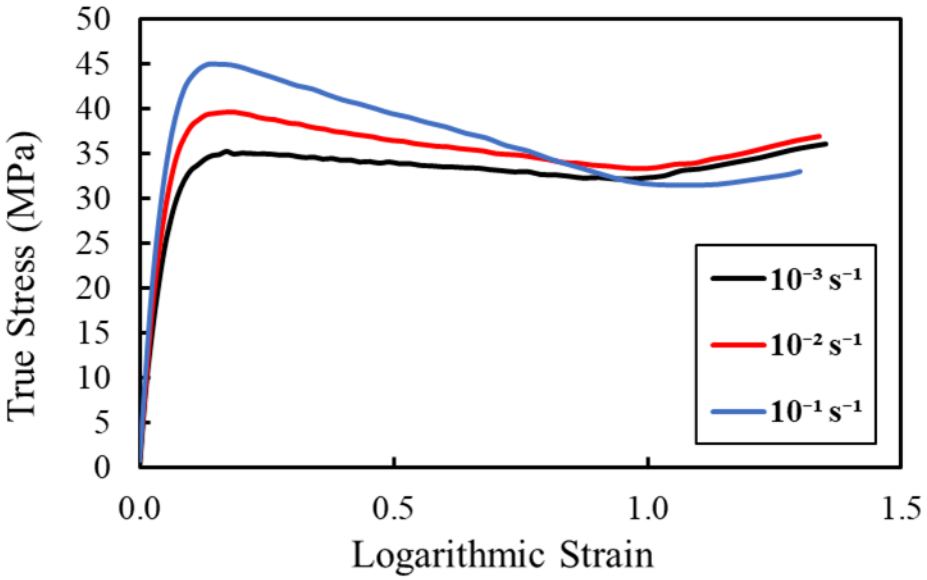

Figure 2.2. True stress versus logarithmic strain in compression for isotactic polypropylene homopolymer for three different strain rates.

All samples are compressed to a logarithmic strain of 1.3 mm/mm. Three specimens are tested for each input strain rate. The experimental results are reported in Fig. 2.2.

The experimental true stress versus true strain response for all three rates includes yielding followed by a softening phase and subsequent strain hardening phase at a strain between 1.0 and 1.2 mm/mm. It is worth noting, that many semicrystalline polymers do not exhibit a strain softening phase in compression. In an earlier work, [7] measured the internal temperature of polypropylene specimens subjected to compression across a wide range of strain rates. It was found that the internal temperature increases during the onset of plastic deformation and determined that this increase in temperature is responsible for the macro softening response.

2.2.4 Notched cylindrical tensile bar testing

Samples for the notched cylindrical bars are machined in the longitudinal direction with dimensions shown below in Fig. 2.3. Three samples for each notch radius, R, are tested for input strain rate values of 10^{-4} s^{-1}, 10^{-3} s^{-1}, 10^{-2} s^{-1}, and 10^{-1} s^{-1} respectively.

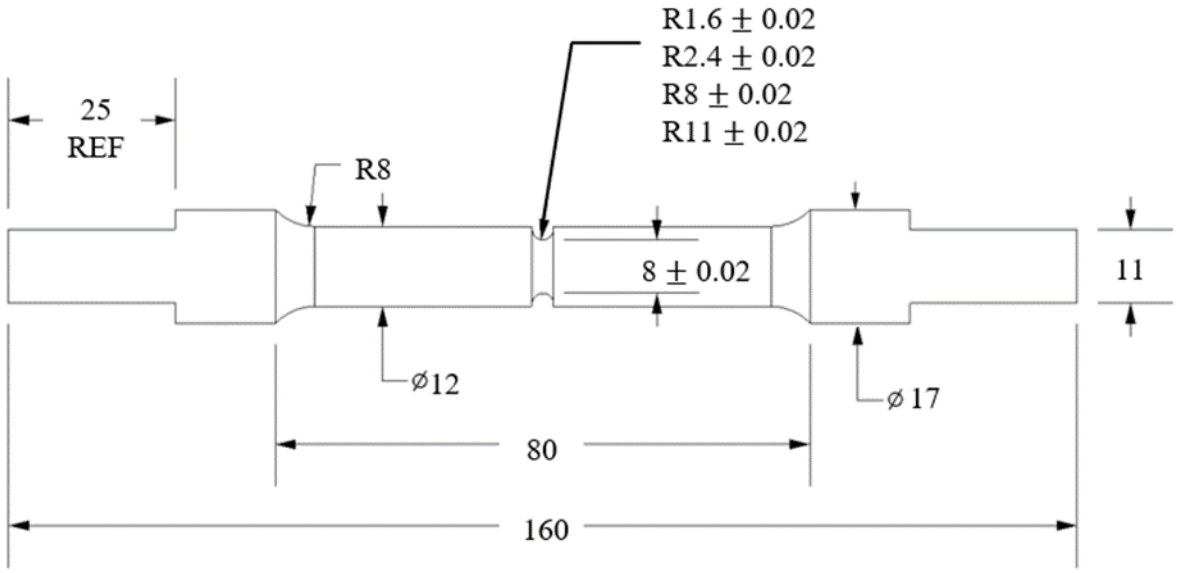

Figure 2.3. Geometry and dimensions of the notched cylindrical tensile bars.

The maximum triaxiality value η and the critical failure strain ε_c are calculated as,

$$\eta = \frac{\sigma_m}{\sigma_{eq}} = \frac{1}{3} + ln\left(1 + \frac{D_0}{4R}\right)$$
$$\varepsilon_c = 2ln\left(\frac{D_0}{D_c}\right) \tag{2.1}$$

where σ_m is the mean stress and σ_{eq} is defined as the von Mises equivalent stress. D_0 = 8.0 mm is the minimum section diameter that remains unchanged for all tensile bars. ε_c is defined as the critical failure strain, calculated as a function of the experimentally measured section diameter at fracture, D_c. The measured failure strain data for the notched cylindrical bar testing are shown below in Fig. 2.4.

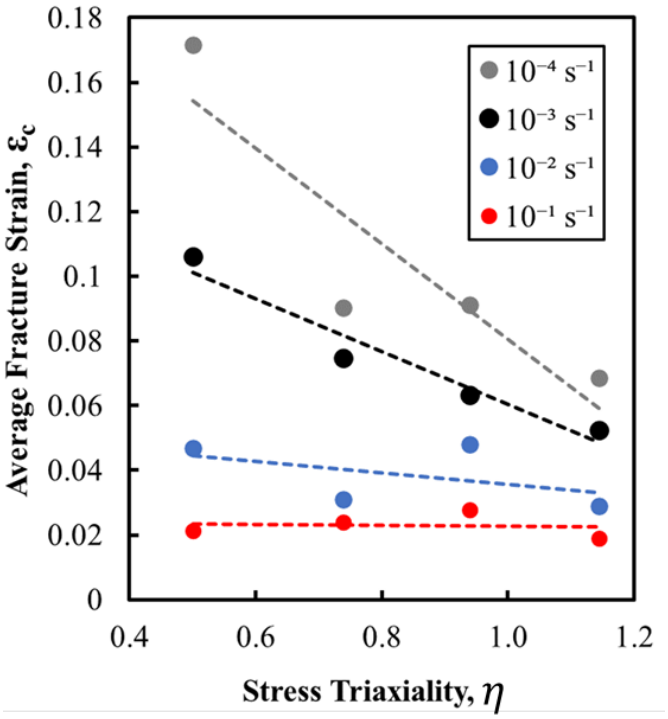

Figure 2.4. Average fracture strain, ε_c versus stress triaxiality, η .

In general, the constitutive behavior of semicrystalline polymers are rate and pressure sensitive. For isotactic polypropylene (as well as many other semicrystalline polymers), cavitation induced damage initiation around the yield-point is driven by the hydrostatic tensile stress state. In Fig. 4, for the notched cylinder, rate dependent tension test data, it is observed that higher triaxiality ratios (corresponding to higher hydrostatic stress) result in lower fracture strain. Further at higher strain rates as the material becomes less ductile lower fracture strain is measured, and an overall decrease in the sensitivity to the triaxiality ratios is noted. However, for lower strain rates, we see higher fracture strains indicating more ductile behavior, and higher sensitivity to triaxiality.

2.2.5 Tensile testing of a thin plate with circular hole

Samples for the thin plate with circular hole are machined in the longitudinal direction with dimensions shown below in Fig. 2.5. Nominal dimensions of the specimens are 75 mm x 40 mm, with a plate thickness of 1.9 mm and a hole diameter of 12 mm.

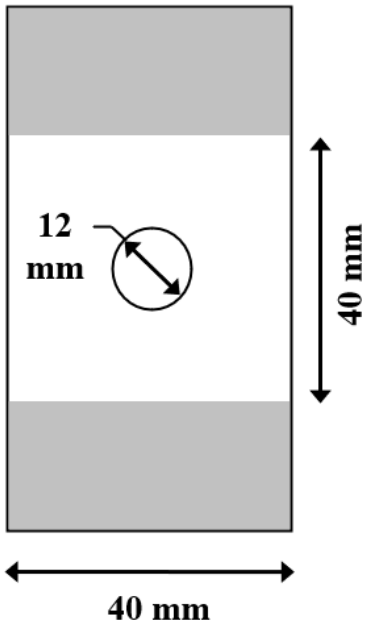

Figure 2.5. Plate with a circular hole geometry.

The grip length is set for each sample at 40 mm and screw action grips are used to ensure grip sliding does not occur during testing. All samples were similarly tested with crosshead control at the same three respective strain rates (10^{-3} s^{-1}, 10^{-2} s^{-1}, and 10^{-1} s^{-1}). A video

extensometer system (MTS AVX Advantage Video System) is used to capture the force-displacement response, as well as DIC results for strain values at the notch.

Fig. 2.6 shows the experimental results for the measured force-displacement curves for each respective strain rate.

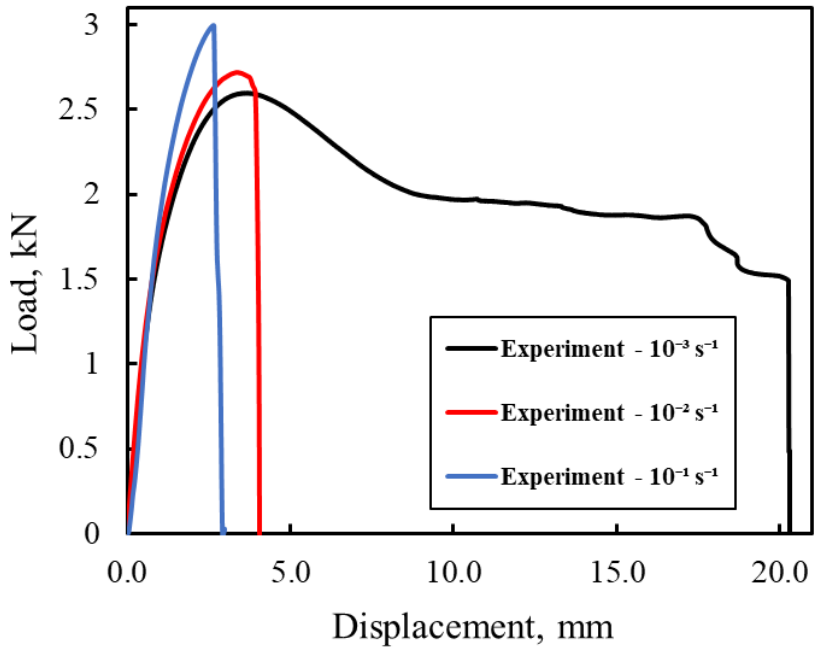

Figure 2.6. Experimental force-displacement curves for the thin plate with circular hole.

For the DIC testing, the quality of the imaging is directly related to the quality of the speckle pattern applied to the surface. Given that polypropylene is often a poor paint substrate for paint application, it was found that several trial experiments with the speckle pattern was required to optimize the results. For our study, a combination of an adhesion promoter plus a black aerosol spray paint worked best. This required a careful application

of paint, sprayed from a distance of approximately 0.5 meters. It is noted that is very important to make sure excess paint does not accumulate as the DIC software will tend to yield a breakup of the strain map, resulting in lower quality gradients. Fig. 2.7 below shows the DIC experimental strain gradient ε_{22}, for reference strain of 10^{-1} s^{-1}.

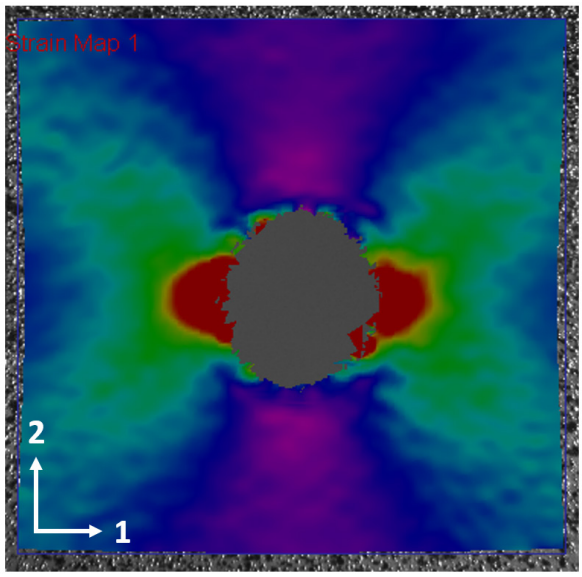

Figure 2.7. DIC for strain (ε_{22}) for the thin plate with circular hole.

2.2.6 Three-point bend testing of a notched beam

Samples for the three-point bend samples are machined in the longitudinal direction and tested at the same three input strain rates. Fig. 2.8 below, shows the sample geometry and nominal dimensions for a nominal beam thickness of 12.5 mm.

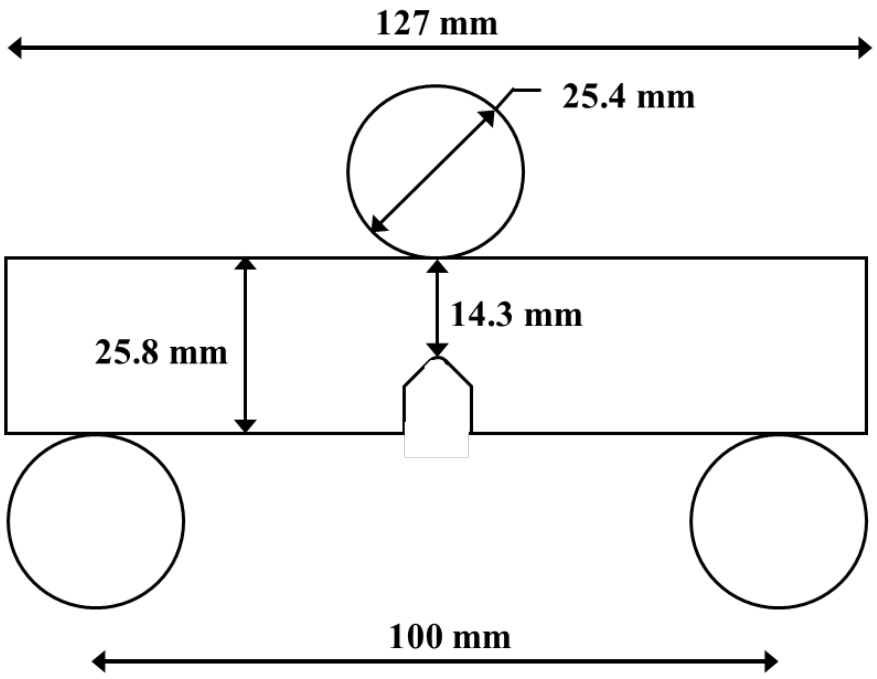

Figure 2.8. Notched three-point bend beam geometry.

Crosshead controlled tests are conducted for all test specimens and tested following ASTM D5045 as a standard for plane-strain fracture testing. A sample size of three is used for each input strain rate and the video extensometer system (MTS AVX Advantage Video System) is used to capture the force-displacement response, as well as DIC results for strain values at the notch.

Fig. 2.9 shows the experimental results for the measured force-displacement curves for each respective strain rate.

For the DIC testing, the same approach outline in section 2.2.5 was used to apply the speckle patter to the samples. The results for the DIC testing is shown below in Fig. 2.10 below,

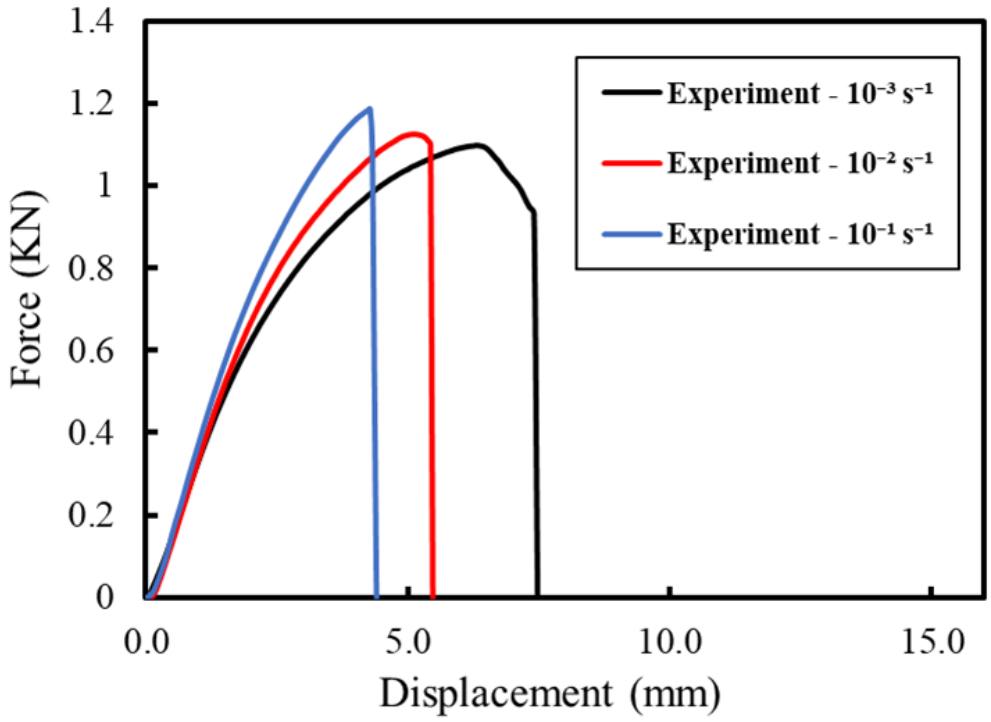

Figure 2.9. Experimental force-displacement curves for the notched beam in three-point bending.

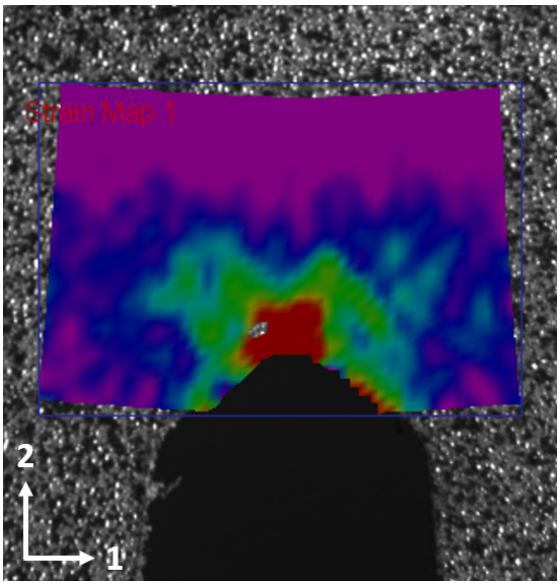

Figure 2.10. DIC for strain (ε_{11}) for the notched beam in three-point bending.

2.3 Constitutive model for semicrystalline polymer

2.3.1 Kinematics of deformation

In the present work the notation used is based on the standard of continuum mechanics [5]. Consider a homogeneous body B_R identified with the region of space it occupies in a fixed reference configuration, and denote **X** for an arbitrary material point of B_R, then the motion

of B_R is a smooth one-to-one mapping of $\boldsymbol{x} = \boldsymbol{\chi}(\mathbf{X}, t)$ with the deformation gradient defined as,

$$\boldsymbol{F} = \frac{\partial \boldsymbol{\chi}}{\partial \mathbf{X}} \tag{2.2}$$

such that $J = det\, \boldsymbol{F} > 0$.

An essential ingredient of elastic-viscoplastic constitutive theories for polymers is the multiplicative decomposition of $\boldsymbol{F}$ as,

$$\boldsymbol{F} = \boldsymbol{F}^e \boldsymbol{F}^p \tag{2.3}$$

into the elastic component, $\boldsymbol{F}^e$, and the irreversible plastic component, $\boldsymbol{F}^p$ [4], which incorporates the permanent viscoplastic deformation that occurs in semicrystalline polymers. This additionally assumes that the Jacobians,

$$J^e = det\, \boldsymbol{F}^e > 0 \quad \text{and} \quad J^p = det \boldsymbol{F}^p > 0 \tag{2.4}$$

are both greater than zero, so that both $\boldsymbol{F}^e$ and $\boldsymbol{F}^p$ are invertible as shown in Eq. 2.4 above. Per the standard, the right and left polar decompositions of $\boldsymbol{F}^e$ and $\boldsymbol{F}^p$ are given by,

$$\boldsymbol{F}^e = \boldsymbol{R}^e\boldsymbol{U}^e = \boldsymbol{V}^e\boldsymbol{R}^e \text{ and } \boldsymbol{F}^p = \boldsymbol{R}^p\boldsymbol{U}^p = \boldsymbol{V}^p\boldsymbol{R}^p \tag{2.5}$$

where $\boldsymbol{R}^e$, $\boldsymbol{R}^p$ are the rotations and $\boldsymbol{U}^e$,$\boldsymbol{U}^p$, $\boldsymbol{V}^e$, $\boldsymbol{V}^p$ are symmetric, positive-definite tensors with,

$$\begin{aligned} \boldsymbol{U}^e &= \sqrt{\boldsymbol{F}^{e^T}\boldsymbol{F}^e}\,, \quad \boldsymbol{V}^e = \sqrt{\boldsymbol{F}^e\boldsymbol{F}^{e^T}} \\ \boldsymbol{U}^p &= \sqrt{\boldsymbol{F}^{p^T}\boldsymbol{F}^p}, \quad \boldsymbol{V}^p = \sqrt{\boldsymbol{F}^p\boldsymbol{F}^{p^T}} \end{aligned} \tag{2.6}$$

The right and left elastic and plastic Cauchy-Green tensor are likewise given by,

$$\begin{aligned} \boldsymbol{C}^e &= \boldsymbol{U}^{e\,2} = \boldsymbol{F}^{e^T}\boldsymbol{F}^e, \qquad \boldsymbol{B}^e = \boldsymbol{V}^{e\,2} = \boldsymbol{F}^e\boldsymbol{F}^{e^T} \\ \boldsymbol{C}^p &= \boldsymbol{U}^{p\,2} = \boldsymbol{F}^{p^T}\boldsymbol{F}^p, \qquad \boldsymbol{B}^p = \boldsymbol{V}^{p\,2} = \boldsymbol{F}^p\boldsymbol{F}^{p^T} \end{aligned} \tag{2.7}$$

Further, the velocity gradient is introduced as,

$$\boldsymbol{L} = \dot{\boldsymbol{F}}\boldsymbol{F}^{-1} \tag{2.8}$$

Substituting Eq. 2.3 into the velocity gradient, Eq. 2.8, we get,

$$\boldsymbol{L} = \dot{\boldsymbol{F}}\boldsymbol{F}^{-1} = \dot{\boldsymbol{F}}^e\boldsymbol{F}^{e^{-1}} + \boldsymbol{F}^e\boldsymbol{L}^p\boldsymbol{F}^{e^{-1}} \tag{2.9}$$

with,

$$\boldsymbol{L^e} = \dot{\boldsymbol{F}}^{\boldsymbol{e}}\boldsymbol{F}^{e\,-1} \text{ and } \boldsymbol{L^p} = \dot{\boldsymbol{F}}^{\boldsymbol{p}}\boldsymbol{F}^{p\,-1} \qquad 2.10)$$

The elastic and plastic deformation tensor can be further defined from standard continuum mechanics as,

$$\boldsymbol{D}^e = sym\,\boldsymbol{L}^e,\ \boldsymbol{W}^e = skw\,\boldsymbol{L}^e, \quad \text{and } \boldsymbol{D}^p = sym\,\boldsymbol{L}^p,\ \boldsymbol{W}^p = skw\,\boldsymbol{L}^p \qquad (2.11)$$

so that $\boldsymbol{L}^e = \boldsymbol{D}^e + \boldsymbol{W}^e$ and $\boldsymbol{L}^p = \boldsymbol{D}^p + \boldsymbol{W}^p$. Assuming plastic flow is incompressible and irrotational such that,

$$J^p = det\boldsymbol{F}^p = 1\,, \qquad \text{tr } \boldsymbol{L}^p = 0 \quad \text{and} \quad \boldsymbol{W}^p = 0 \qquad (2.12)$$

then the plastic velocity gradient is then defined as $\boldsymbol{L}^p \equiv \boldsymbol{D}^p$. This follows that the evolution law for the plastic part of the deformation gradient can be written as:

$$\dot{\boldsymbol{F}}^p = \boldsymbol{D}^p\,\boldsymbol{F}^p \qquad (2.13)$$

2.3.2 Free energy

To state the specific form for free energy, it is helpful to first define the effective distortional plastic stretch, λ^p as,

$$\lambda^p = \frac{1}{\sqrt{3}}\sqrt{tr(\boldsymbol{B}^p)} \tag{2.14}$$

where the plastic component of the left Cauchy-Green tensor, $\boldsymbol{B}^p$, is defined in Eq. (2.7). Following which, the non-interactive form of the Helmholtz free energy is defined as,

$$\psi = \psi^e(\boldsymbol{E}^e) + \psi^p(\lambda^p) \tag{2.15}$$

where ψ^e and ψ^p are the elastic and plastic free energies, respectively. $\boldsymbol{E}^e$ is the elastic Green strain tensor, given as,

$$\boldsymbol{E}^e = \frac{1}{2}(\boldsymbol{C}^e - \boldsymbol{I}) \tag{2.16}$$

where the elastic right Cauchy-Green tensor, $\boldsymbol{C}^e$, is also defined in Eq. (2.7).

For the elastic free energy, attention is restricted to the standard form for small elastic stretches as,

$$\psi^e(\boldsymbol{E}^e) = G|\boldsymbol{E}_0^e|^2 + \frac{1}{2}K|tr\boldsymbol{E}^e|^2 \tag{2.17}$$

where G and K are the shear and bulk moduli, respectively. $\boldsymbol{E}_0^e$ is the deviatoric component of the elastic Green strain as,

$$\boldsymbol{E}_0^e = \boldsymbol{E}^e - \frac{1}{3}(tr\,\boldsymbol{E}^e)\boldsymbol{I} \tag{2.18}$$

For the plastic free energy, it is assumed that ψ^p arises from an entropic contribution of the molecular entanglement in the amorphous region [18]. Additionally, the plastic energy continues to change during the orientation hardening phase of large deformation where the crystalline and amorphous regions untangle and begin to align [31]. Since this is very similar to the rubbery network-like response of glassy polymers experienced during plastic deformation, the statistical mechanics model from [4] is considered to model the plastic energy as,

$$\psi^p = \mu_R\lambda_L^2\left[\left(\frac{\lambda^p}{\lambda_L}\right)x + ln\left(\frac{x}{\sinh x}\right) - \left(\frac{1}{\lambda_L}\right)y - ln\left(\frac{y}{\sinh y}\right)\right] \tag{2.19}$$

where the material constants μ_R and λ_L are the material rubbery modulus and the network locking stretch respectively. x and y are defined as

$$x = \mathcal{L}^{-1}\left(\frac{\lambda^p}{\lambda^L}\right) \quad \text{and} \quad y = \mathcal{L}^{-1}\left(\frac{1}{\lambda_L}\right) \tag{2.20}$$

Note that $\mathcal{L}^{-1}$ is the inverse of the Langevin function.

2.3.3 Equation for stress and back stress

Following the free energy defined in Eq. (2.17), the second Piola-Kirchoff stress is given by,

$$\boldsymbol{S}^e = \frac{\partial \psi^e}{\partial \boldsymbol{E}^e} = 2G\boldsymbol{E}_0^e + K(tr\boldsymbol{E}^e)\boldsymbol{I} \tag{2.21}$$

Pulling forward from the referenced condition, the Cauchy stress is then defined as,

$$\boldsymbol{T}^e = J\boldsymbol{F}^{e\,-1}\boldsymbol{S}^e\boldsymbol{F}^{e-T} \tag{2.22}$$

Following the approach of Anand and Gurtin [4], the driving force for plastic flow is further defined as,

$$(\boldsymbol{S}_0^e)_{eff} = \boldsymbol{S}_0^e - \boldsymbol{S}_{back}, \quad \text{with} \quad \boldsymbol{S}_0^e = \boldsymbol{S}^e - \frac{1}{3}(tr\,\boldsymbol{S}^e)\boldsymbol{I} \tag{2.23}$$

where $(\boldsymbol{S}_0^e)_{eff}$ is defined as the "effective" second Piola-Kirchoff deviatoric elastic stress that accounts for a difference between the deviatoric stress tensor $\boldsymbol{S}_0^e$, and an evolving back stress tensor, $\boldsymbol{S}_{back}$. The back stress tensor represents an internal "resistance" experienced during the molecular alignment phase. This assumption is supported physically as it is well known that semicrystalline polymers experience the same type of morphology evolution as amorphous polymers during the molecular realignment phase. To ensure a thermodynamically consistent theory, the back-stress definition is used following [4] as,

$$\boldsymbol{S_{back}} = 2sym_0\left(\frac{\partial \psi^p}{\partial \boldsymbol{B}^p}\right)\boldsymbol{B}^p = \mu \boldsymbol{B}_0^p, \quad \text{where} \quad \boldsymbol{B}_0^p = -\frac{1}{3}(tr\ \boldsymbol{B}^p)\boldsymbol{I} \tag{2.24}$$

where the back-stress modulus, μ is defined by

$$\mu = \frac{1}{3\lambda^p}\frac{\partial \psi^p}{\partial \lambda^p} = \mu_R \frac{\lambda_L}{3\lambda^p}\mathcal{L}^{-1}\left(\frac{\lambda^p}{\lambda_l}\right) \tag{2.25}$$

and $\boldsymbol{B}_0^p$ is defined as deviatoric component of the left plastic Cauchy-Green tensor.

Using the Padé approximation for the Langevin function, the back stress modulus then becomes

$$\mu = \mu_R \frac{\lambda_L}{3\lambda^p}\frac{\lambda^p}{\lambda_L}\left(\frac{3 - \left(\frac{\lambda^p}{\lambda_L}\right)^2}{1 - \left(\frac{\lambda^p}{\lambda_L}\right)^2}\right) \tag{2.26}$$

2.3.4 Flow rule

Several flow rules have been developed over the past 80 years that consider plastic flow in a polymer as a thermally activated process [6, 21, 49]. Much of the existing literature focuses on flow rules for the amorphous polymers. Semicrystalline polymers are often more complex in their macroscale plastic flow, and additionally more sensitive to the processing conditions, making it more difficult to get consistent test results. In this paper, a thermally activated flow rule originally used for amorphous materials [5] is adopted. This flow rule offers a rate and temperature-dependent yield strength function that adopts an activation energy-based approach for the onset of plastic flow. Because the amorphous and crystalline phases contribute together in the macroscopic deformation, and the onset of plastic flow is driven by the movement of the amorphous regions between the lamellae, it is reasonable to assume that an activation energy approach might work for a semicrystalline material. From Eq. 2.13 the flow rule is defined as,

$$\dot{\boldsymbol{F}}^p = \boldsymbol{D}^p \boldsymbol{F}^p \text{ where } \boldsymbol{F}^p(\boldsymbol{X}, 0) = 1 \tag{2.27}$$

Then, following [4], and [2], the inelastic stretch rate is given by a standard Mises-type flow rule defined as,

$$\boldsymbol{D}^p = \dot{\gamma^p} \left(\frac{(\boldsymbol{S}_0^e)_{eff}}{2\bar{\tau}} \right) \tag{2.28}$$

where $(\boldsymbol{S}_0^e)_{eff}$ is defined in Eq. (2.23) and $\dot{\gamma^p}$ is defined as the equivalent plastic shear-strain rate. $\bar{\tau}$ is the equivalent shear stress defined by:

$$\bar{\tau} = \frac{1}{\sqrt{2}} \left| (\boldsymbol{S}_0^e)_{eff} \right| \tag{2.29}$$

Here, $|\boldsymbol{A}| = \sqrt{\boldsymbol{A} : \boldsymbol{A}}$ denotes the magnitude of a second order tensor $\boldsymbol{A}$. Further, the quantity

$$\varepsilon_{eq}^p = \int_o^t \sqrt{\boldsymbol{D}^p : \boldsymbol{D}^p}\, dt \tag{2.30}$$

is defined as the equivalent plastic shear strain rate and is used as a scalar measure to quantify the amount of plastic strain accumulated at time t. To leverage the thermally activated mechanism following the work of [2], $\dot{\gamma^p}$ is defined as,

$$\dot{\gamma^p} = \begin{cases} 0 & \text{if} \quad \tau_e \leq 0 \\ \dot{\gamma_0} exp\left\{\frac{Q}{-k_B \vartheta}\right\} \left[sinh\left(\frac{\tau_e V}{2k_B \vartheta}\right)\right]^{\frac{1}{m}} & \text{if} \quad \tau_e \geq 0 \end{cases} \tag{2.31}$$

where,

$$\tau_e \stackrel{\text{def}}{=} \bar{\tau} - \left(S_1 + \alpha_p \bar{p}\right), \qquad with \quad \bar{p} = -\frac{1}{3}(tr\, \boldsymbol{S}^e)\boldsymbol{I} \tag{2.32}$$

τ_e is defined as the net shear stress for thermally activated flow. α_p is a parameter that is used to account for the pressure sensitivity of plastic flow [48] and $\bar{p}$ is defined as the mean normal pressure. $\dot{\nu_0}$ is defined as the reference shear strain parameter with the units of s^{-1}.

Q is defined as the activation energy, k_B is Boltzmann's constant, V is an activation volume, and m is the strain rate sensitivity parameter. S_1 is the internal plastic variable that will be explained later in section 2.3.5. It should be noted that the flow rule in Eqn. 23 can exploit temperature dependency of the plastic shear strain rate in terms of the parameter ϑ. However, the present study is limited only to predict isothermal response for semicrystalline polymers at room temperature.

2.3.5 Evolution of the internal plastic variables, S_1 and ϕ

Two internal variables S_1 and ϕ are defined to represent aspects of the intermolecular shear resistance to plastic flow experienced during the "yield-peak" observed in amorphous and semicrystalline materials, where the yield-peak is defined as the peak stress experienced after plastic yielding but before a softening ensues. $\phi \geq 0$ is a dimensionless parameter that represents the local change in molecular-packing due to deformation-induced disordering, whereas $S_1 \geq 0$ represents a transient resistance to plastic flow coupled to the disordering of the material. Following [2], it is assumed that a very small microscale dilatation occurs during plastic deformation as the material disorders but still maintains an incompressible plastic flow. This results in an increase of the order parameter ϕ and causes a transient change to the flow resistance S_1 of the material as plastic deformation proceeds. Accordingly, the evolution of the resistance S_1 is coupled to the evolution of the order-parameter ϕ.

For the internal plastic variables, the following coupled evolution equations are defined according to [2] as,

$$\dot{S_1} = h_1(S_1^* - S_1)\dot{\gamma^p}, \quad \text{with the initial value} \quad S_1(\boldsymbol{X}, 0) = S_{1i}$$
$$S_1^* = b(\phi^* - \phi) \tag{2.33}$$

and

$$\dot{\phi} = g(\phi^* - \phi)\dot{\gamma^p}, \quad \text{with the initial value} \quad \phi(\boldsymbol{X}, 0) = \phi_i \tag{2.34}$$

For the flow resistance in Eq. (2.33), the function $h_1(S_1^* - S_1)$ represents a strain hardening/softening function for the resistance S_1 , where S_1^* is defined as a saturation value to the flow stress and h_1 is a material constant that controls the initial slope of the yield-peak (as h_1 increases, the initial yield slope increases). Accordingly, the material hardens if $S_1 \leq S_1^*$ and softens if $S_1 \geq S_1^*$.

For the order parameter defined in Eq. (2.34), the function $g(\phi^* - \phi)$ represents a shear induced disorder function for the parameter ϕ, where ϕ^* is defined as a saturation value of the parameter and g is a material constant that controls the width of the yield peak (as g decreases, the yield-peak width narrows). Accordingly, the material disorders if $\phi \leq \phi^*$ and becomes less disordered if $\phi \geq \phi^*$.

S_1^* represents a coupling function between the flow resistance S_1 and the order parameter ϕ that controls the magnitude of the stress overshoot. Here, b and the saturation limit ϕ^* both represent material parameters that control the height of the yield peak (as ϕ^* or b increases, the yield peak also increases).

Hence, we get a combined list of material parameters for the evolution equations defined as $\{h_1, b, \phi^*, g\}$ that needed to be determined from the experimental data to phenomenologically model the yield-strength for both tension and compression.

2.3.6 Damage model for semicrystalline polymers

In order to model the cavitation induced damage in semicrystalline polypropylene during rate dependent tensile loading, a damage model originally proposed by [47] is used as a starting basis. The original Rice-Tracey model considered a single void growth under a super imposed hydrostatic stress. The original model was later modified by [57, 58] to include the effect of neighboring void growth and coalescence as,

$$\frac{dR}{R} = exp(\beta\eta)d\varepsilon_{eq}^{p} \tag{2.35}$$

where R is expressed as the average void radius, β is a constant to reflect the interaction of neighboring voids, $\eta = \frac{\sigma_m}{\sigma_e}$ is the stress triaxiality ratio with σ_m as the hydrostatic stress

and σ_e as the von Mises equivalent stress, and ε_{eq}^{p} is defined as the equivalent plastic strain. Experimental results from [58] showed that the fracture strain of polycarbonate decreased with an increase in triaxiality and a critical void growth ratio based on the Rice-Tracey model could be used as a stress-state independent micromechanics fracture criterion as,

$$\left(\frac{dR}{R}\right)_c = exp(\beta\eta)\varepsilon_c^p \tag{2.36}$$

where $\varepsilon_c^P = 2ln\left(\frac{D_0}{D_c}\right)$ is defined as the critical equivalent plastic strain at fracture, D_0 is the minimum section diameter, and D_c is defined as the critical section dimeter measured right after the specimen fractures. It should be mentioned here that the proposed micromechanics parameter from Wang and Kishimoto [58] for ductile damage initiation only includes stress states of the notched bar with varied geometry, as shown in Fig. 2.3. and does not consider the effect of input strain rate. By contrast, the present study is aimed at formulating a rate-dependent isotropic damage evolution law, coupled with viscoplasticity, that uses the same micromechanics parameter for various stress states for the constitutive model outlined in sections 2.3.1 to 2.3.5, for polypropylene.

Hence, considering the rate dependent form of Eq. (2.35), a simple evolution equation for the damage variable, d is given as,

$$\dot{d} = \exp(\beta\eta)\dot{\gamma_d^p} \tag{2.37}$$

where the rate of damage growth is a function of triaxiality η, the rate dependent constant β, (to represent the interaction of neighboring voids), and the damaged equivalent shear strain rate, $\dot{\gamma_d^p}$. The physical motivation for $\dot{\gamma_d^p}$ is presented as follows: Once damage begins to evolve, the elastic energy starts dropping, causing the stress to drop. This can cause a non-physical situation of pulling back the stress within the yield surface. To avoid this, the plastic strain evolution needs to incorporate a damage counterpart as derived below, which eventually makes the damage evolution law also coupled via γ_d^p. Therefore, the modified flow rule is considered as,

$$\boldsymbol{D}^p = \dot{\gamma_d^p} \frac{dF}{d\boldsymbol{S}_D} \tag{2.38}$$

where F represents the yield function and $\boldsymbol{S}_D$ represents the damaged stress as,

$$\boldsymbol{S}_D = (1-d)^2\, \boldsymbol{S} \tag{2.39}$$

where $(1-d)^2$ is defined as a monotonically decreasing degradation function that degrades the elastic energy storage in the material neighborhood. $\boldsymbol{D}^p$ is further defined as,

$$\boldsymbol{D}^p = \dot{\gamma^p}\left(\frac{dF}{d\boldsymbol{S}}\right)\frac{d\boldsymbol{S}}{d\boldsymbol{S}_D} = \dot{\gamma^p}\left(\frac{1}{(1-d)^2}\right)\frac{dF}{d\boldsymbol{S}}, \quad \text{as} \quad \frac{d\boldsymbol{S}}{d\boldsymbol{S}_D} = \frac{1}{(1-d)^2} \tag{2.40}$$

leading to a flow rule affected by the damage growth as,

$$\boldsymbol{D}^p = \frac{\dot{\gamma^p}}{(1-d)^2}\left(\frac{dF}{d\boldsymbol{S}}\right) \tag{2.41}$$

Equivalently, the damaged equivalent plastic shear strain rate is now defined as,

$$\dot{\gamma_d^p} = \frac{\dot{\gamma^p}}{(1-d)^2} \tag{2.42}$$

leading to the final coupled damage evolution equation as,

$$\dot{d} = \exp(\beta\eta)\frac{\dot{\gamma^p}}{(1-d)^2} \tag{2.43}$$

The elastic energy density for the damaged material is further expressed as,

$$\psi_e^D(\boldsymbol{E}^e) = (1-d)^2\left[G|\boldsymbol{E}_0^e|^2 + \frac{1}{2}K|tr\boldsymbol{E}^e|^2\right] \tag{2.44}$$

which then leads to the elastic stress of the damaged material as,

$$\boldsymbol{S}^{eD} = \frac{\partial\psi_e^D}{\partial\boldsymbol{E}^e} = (1-d)^2[2G\boldsymbol{E}^e + \lambda(tr\,\boldsymbol{E}^e)\mathbf{I}] \tag{2.45}$$

Additionally, the damaged net shear stress for thermally activated flow is defined as,

$$\tau_e{}^D \overset{\text{def}}{=} \bar{\tau} - (1-d)^2 S_1 - \alpha_p\bar{p} \tag{2.46}$$

where the degradation function is applied to the flow stress as well.

The damage model can now be summarized as follows - in the first stage, the cavitation induced damage initiates and becomes fully developed, which is controlled by a critical value of the equivalent plastic strain, ε_i^p. The physical significance of ε_i^p can be explained as a certain amount of latent plasticity being required to build up during the onset of the plastic yielding controlling the damage initiation. This value of ε_i^p is determined iteratively by trial and error, while comparing the numerical simulations to the experimental force-displacement curves for tensile test results. Thus, it is considered that damage evolution starts when the equivalent plastic strain ε_{eq}^preaches the initiation value ε_i^p for strain rates above $10^{-3}\ s^{-1}$.

$$\varepsilon_{eq}^p \geq \varepsilon_i^p, \quad \text{for } \dot{\varepsilon} \geq 10^{-3}\ s^{-1} \tag{2.47}$$

However, below this rate, the deformation is dominated by a shear yielding mechanism with a large amount of stretching and cavitation induced damage is not active. Following the initiation, the second stage of damage growth is controlled by the evolution equation defined in Eq. (2.43). Finally, the third stage, driven by fibrillation and molecular chain-scission until the complete fracture, is considered when the damage parameter, d reaches a critical value d_c, as,

$$d \leq d_c, \quad \text{for } \dot{\varepsilon} \geq 10^{-3}\, s^{-1} \tag{2.48}$$

which is also limited by the applied strain rate as given in Eq. (2.48). The value of d_c is similarly estimated by trial and error, while comparing the numerical simulations to the experimental results obtained for the tensile bar.

Recognizing that the damage response based on the proposed continuum level model would be mesh-dependent in the finite element simulations, a mesh sensitivity study is performed to determine the smallest element size. The information about the mesh density required to obtain mesh-objective results corresponding to each simulation domain has been presented in section 2.5.

2.4 Estimation of the material parameters for polypropylene

In this section, the parameter estimation procedure is discussed for the proposed constitutive model. In summary, the following parameters are determined for both tension and compression:

1. The shear and bulk moduli (G, K) in the elastic free energy.

2. The parameters (μ_R, λ_L) in the plastic free energy.
3. The pressure sensitivity parameter, (α).
4. The parameters $\{Q, V, \dot{\gamma}_0, m, S_1, h_1, b, g_1, \phi^*\}$ for the flow rule and the evolution equations of the internal variables.
5. The parameters $(\varepsilon_i^p, \beta, d_c)$ in the damage model.

It is well known that the elastic parameters of polymers often vary in tension versus compression. The Young's modulus and Poisson's ratio, ν, are determined from the testing outlined in section 2.2. Standard relations for isotropic elasticity are then used to determine the shear modulus, G, and the bulk modulus, K, for tension and compression, as given by,

$$\nu = 0.36, \quad E_T = 1230\ MPa, \quad E_C = 733\ MPa$$

$$K_T = 1464\ MPa, \quad K_C = 873\ MPa$$

From here, the average values of the elastic modulus are computed and used in the simulations as,

$$G_{avg} = 361\ MPa, \quad K_{avg} = 1168\ MPa$$

For the estimation of the pressure sensitivity parameter α, an equation developed by [48] is used to compute the sensitivity parameter as a function of the materials yield strength in tension and compression as,

$$\alpha = 3\frac{\sigma_y^C - \sigma_y^T}{\sigma_y^C + \sigma_y^T} \tag{2.49}$$

Following which, the pressure sensitivity parameter is then calculated as:

$$\alpha = 0.284$$

To estimate the parameters required in the flow rule, test data for rate dependent tension and compression are used. Following the approach presented by [2], a one-dimensional small strain approximation is considered for the flow rule defined in Eq. (2.31) and (2.32) as,

$$\dot{\varepsilon}^p = \begin{cases} 0 & \text{if} \quad \sigma_e \leq 0 \\ \dot{\varepsilon}_0 exp\left\{\frac{Q}{-k_B\vartheta}\right\}\left[sinh\left(\frac{\sigma_e V}{2k_B\vartheta}\right)\right]^{\frac{1}{m}} & \text{if} \quad \sigma_e \geq 0 \end{cases} \tag{2.50}$$

$$\sigma_e \overset{\text{def}}{=} \bar{\sigma} - \left(S_1 + \alpha_p \bar{p}\right)$$

with σ_e now defined as the equivalent tensile stress for thermally activated flow. The mean tensile stress $\bar{\sigma}$, and the mean normal pressure $\bar{p}$, are defined as,

$$\bar{\sigma} = |\sigma - \sigma_{back}| \quad \text{and} \quad \bar{p} = -\frac{1}{3}\sigma \tag{2.51}$$

From Eq. (2.50), the pre-hyperbolic constant is set to

$$\varepsilon^*(\vartheta) \stackrel{\text{def}}{=} \dot{\varepsilon_0} \exp\left(-\frac{Q}{K_B\vartheta}\right) \tag{2.52}$$

Subsequently Eq(s). 2.50-2.52 are rearranged into the following form,

$$|\sigma - \sigma_{back}| + \frac{1}{3}\alpha_P\sigma = S_1 + \frac{2K_B\vartheta}{V} sinh^{-1}\left[\left(\frac{\dot{\varepsilon^P}}{\dot{\varepsilon^*}(\vartheta)}\right)^m\right] \tag{2.53}$$

For purpose of obtaining the parameters associated with the yield stress, the contribution of the internal variable S_1 is neglected (which is associated with the transient yield peak), as well as the back stress, σ_{back} (which is associated with the internal resistance experienced during the molecular realignment phase). $|\sigma|$ is set to σ_y where the plastic flow is considered to be fully developed as $\dot{\varepsilon^P} \approx \dot{\varepsilon}$. This results the following approximate expression for the yield stress σ_y as a function of strain rate $\dot{\varepsilon}$ as,

$$\left(1 - \frac{\alpha_P}{3}\right)\sigma_y = \frac{2K_B\vartheta}{V} sinh^{-1}\left[\left(\frac{\dot{\varepsilon}}{\dot{\varepsilon^*}(\vartheta)}\right)^m\right] \tag{2.54}$$

Using Eq. (2.54), parameters $\{V, Q, \dot{\varepsilon_0}, m\}$ are determined experimentally for both tension and compression.

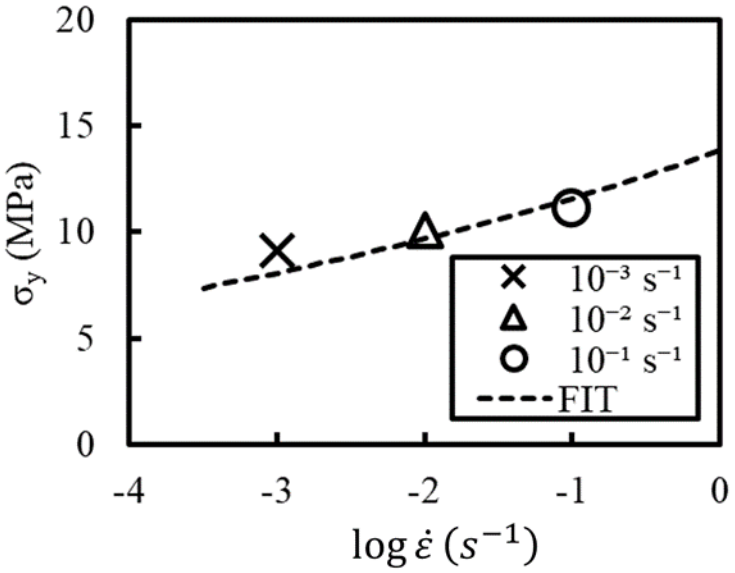

Figure 2.11. Tensile yield stress versus input logarithmic strain rate at room temperature (296 K)

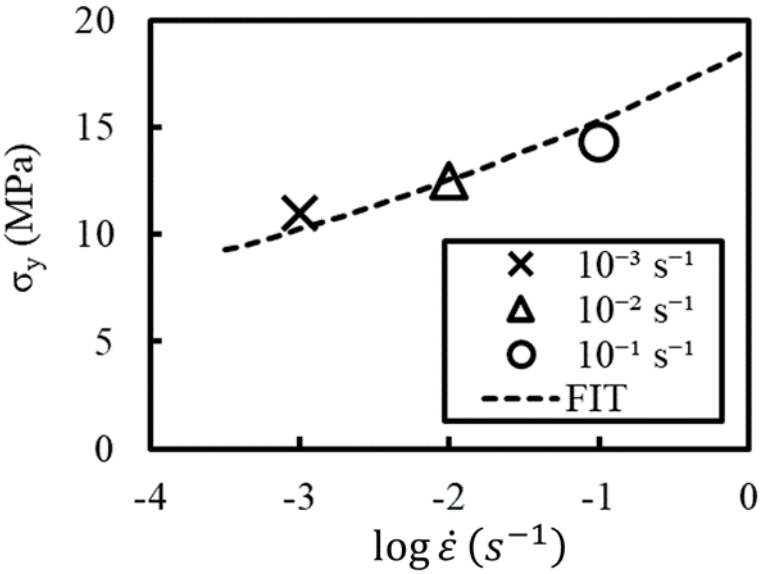

Figure 2.12. Compressive yield stress versus input logarithmic strain rate at room temperature (296 K).

Fig. 2.11 and Fig. 2.12 above show the experimental σ_y versus $log(\dot{\varepsilon})$ plot together with the fitting of Eq. (2.54) for tension and compression, respectively. This yields the following values for tension as,

$$Q = 1.05 \times 10^{-19}\, J, \quad V = 2.30 \times 10^{-28}\, m^3,$$

$$\dot{\varepsilon_0} = \dot{\gamma_0} = 5.10 \times 10^{16}\, s^{-1}, \quad m = .08$$

and for compression as,

$$Q = 1.25 \times 10^{-19}\, J, \quad V = 2.30 \times 10^{-28}\, m^3,$$

$$\dot{\varepsilon_0} = \dot{\gamma_0} = 5.10 \times 10^{16}\, s^{-1}, \quad m = .09$$

As can be seen, the values for the reference strain rate and the activation volume are identical in tension and compression.

The parameters associated with the evolution equations for the plastic variables also need to be calibrated via an empirical fit between the one dimensional model prediction and the uniaxial tension and compression test data obtained in section 2.2.2 and 2.2.3, respectively. For this purpose, the proposed constitutive model outlined in section 2.3 was implemented in ABAQUS/Explicit (ABAQUS 2017) by writing a user subroutine (VUMAT) with an eight-noded brick element (C3D8R). Multiple single element simulations were run to estimate the parameters that provide the best fit between the model and test data. The parameters obtained from this calibration procedure for tension are:

$$S_1 = 0\, MPa, \quad h_1 = 23, \quad b = 5400\, MPa, \quad g_1 = 0.01$$

$$\phi^* = 0.0023, \quad \mu_R = 3.0\, MPa, \quad \lambda_L = 15$$

and for compression as,

$$S_1 = 0, \quad h_1 = 25, \quad b = 1450\ MPa, \quad g_1 = 0.6$$

$$\phi^* = 0.0063, \quad \mu_R = 2.5\ MPa, \quad \lambda_L = 15$$

This initial flow resistance S_1 , and the network locking stretch λ_L, are estimated as identical values for compression and tension. The model predictions as obtained using these calibrated parameters are compared with experimental data as shown below in Fig. 2.13 for tension and in Fig. 2.14 for compression, respectively. It is important to note that one set of parameters has been identified to predict the response at three different strain rates.

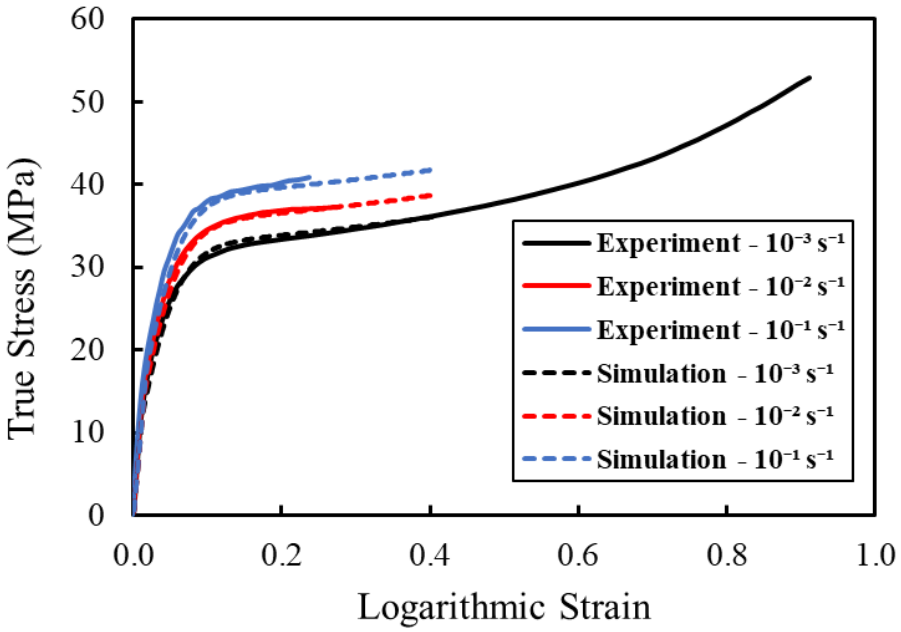

Figure 2.13. Comparison between the calibrated constitutive model and the experimental stress-strain response of the polypropylene in tension.

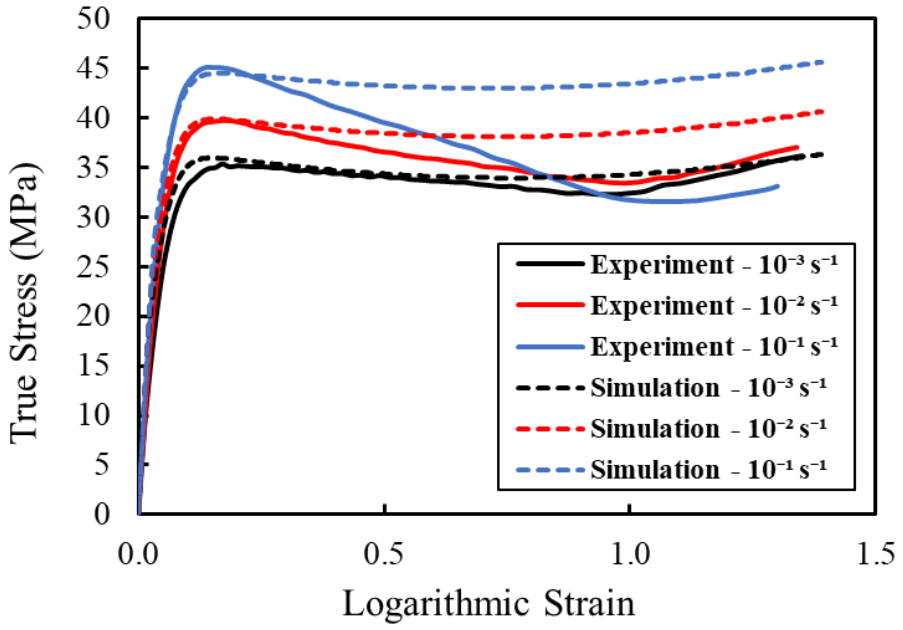

Figure 2.14. Comparison between the calibrated constitutive model and the experimental stress-strain response of the polypropylene in compression.

Table 2.1 below provides a complete summary of the material parameters for the constitutive model.

Table 2-1. Material parameters for polypropylene homopolymer.

Parameter	Description	Tension	Compression
$\boldsymbol{\rho}$ **(tonne/mm^3)**	Density	9.0×10^{-10}	
$\boldsymbol{E_{avg}}$ **(MPa)**	Average Young's modulus	982	
$\boldsymbol{\nu}$	Poisson's ratio	0.36	
$\boldsymbol{G_{avg}}$ $\boldsymbol{(MPa)}$	Average shear modulus	361	
$\boldsymbol{K_{avg}}$ $\boldsymbol{(MPa)}$	Average bulk modulus	1168	
$\boldsymbol{\mu_R}$ **(MPa)**	Rubbery modulus	2.5	3
$\boldsymbol{\lambda_L}$	Network locking stretch	15	
$\boldsymbol{\alpha_P}$	Pressure sensitivity parameter	.284	
$\boldsymbol{\vartheta}$ $\boldsymbol{(K)}$	Room Temperature	296	
Q (J)	Activation energy	1.05×10^{-19}	1.25×10^{-19}
$\boldsymbol{V(m^3)}$	Activation volume	2.3×10^{-28}	
$\boldsymbol{\dot{\gamma}_0(s^{-1})}$	Reference plastic shear-strain rate	5.1×10^{16}	
$\boldsymbol{m}$	Strain rate sensitivity parameter	0.08	0.09
$\boldsymbol{S_1(MPa)}$	IPV: Initial flow resistance	0	
$\boldsymbol{h_1}$	IPV: Flow resistance constant 1	23	25

$\boldsymbol{b}$	IPV: Flow resistance constant 2	5400	1450
$\boldsymbol{g_1}$	IPV: ψ Flow disorder constant	0.01	0.6
$\boldsymbol{\phi^*}$	IPV: ψ Saturation limit	0.0023	0.0063

For the parameters needed in the damage model such as, cavitation induced damage initiation, progressive damage growth, and fibrillation breakdown, the following three-step process is implemented:

Step 1. The cavitation induced damage initiation parameter, ε_i^p, is estimated by repeating the numerical simulations for the tensile bar, considering the plastic parameters listed in Table 2.1 and adjusting the value of ε_i^p to match the yield-point of the experimental load-displacement curve for different strain rates. Correspondingly, values for ε_i^p are estimated as,

$$\varepsilon_i^p = 0.35 \text{ for } \dot{\varepsilon} = 10^{-2}\, s^{-1}, \quad \text{and} \quad \varepsilon_i^p = 0.45 \text{ for } \dot{\varepsilon} = 10^{-1}\, s^{-1}$$

where $\dot{\varepsilon}$ is defined as the input strain rate. Note that the values for ε_i^p are not calculated for rates of $10^{-3}\, s^{-1}$ or less as the damage model is not active during low strain rates, instead the shear-yield mechanism dominates accompanied by large stretches.

Step 2. For the micromechanics fracture criterion expressed in Eq. (2.36), the results from the notched cylindrical bar testing in section 2.2.4 are used to determine the rate dependent, stress state independent parameters $(dR/R)_c$ and β. Given the experimental values of the average fracture strain, ε_c versus triaxiality, η as shown in Fig. (2.4), the critical equivalent plastic strain, $\varepsilon_c^P = 2ln(D_0/D_c)$ is calculated. Next, an assumption is made to enforce a linear fit of average values $(dR/R)_c$ versus η conditioned to a zero slope (i.e. stress-state independence) for each strain rate. Based on this constraint, there exists a unique β for each strain rate. Fig. 2.15 shows the results and variation of the stress-state independent micromechanics fracture criterion, $(dR/R)_c$ vs. triaxiality, η.

Similar to the results of [57] for polycarbonate, the experiments for this work show that $(dR/R)_c$ for polypropylene also exhibits a stress-triaxiality independence but decreases with increasing strain rate for the notched bars as shown in Fig. 2.16. Hence, the approximate function for input strain rate versus β to calibrate the corresponding $(dR/R)_c$ is obtained as,

$$\beta = -0.184ln(\dot{\varepsilon}) - 0.305, \quad \text{for} \quad \dot{\varepsilon} > 10^{-3}\, s^{-1} \tag{2.55}$$

where $\dot{\varepsilon}$ is defined as the input strain rate. This yields the following values for β for the two strain rates as,

$\beta = 0.54$ for $\dot{\varepsilon} = 10^{-2}\, s^{-1}$, and $\beta = 0.12$ for $\dot{\varepsilon} = 10^{-1}\, s^{-1}$, respectively.

Step 3. The critical damage parameter d_c is estimated by repeating the similar numerical trial-error procedure to match the final failure point of the experimental data for the tensile bar. Following which, the d_c values obtained for the two strain rates are as,

$d_c = 0.85$ for $\dot{\varepsilon} = 10^{-2}\, s^{-1}$, and $d_c = 0.61$ for $\dot{\varepsilon} = 10^{-1}\, s^{-1}$, respectively

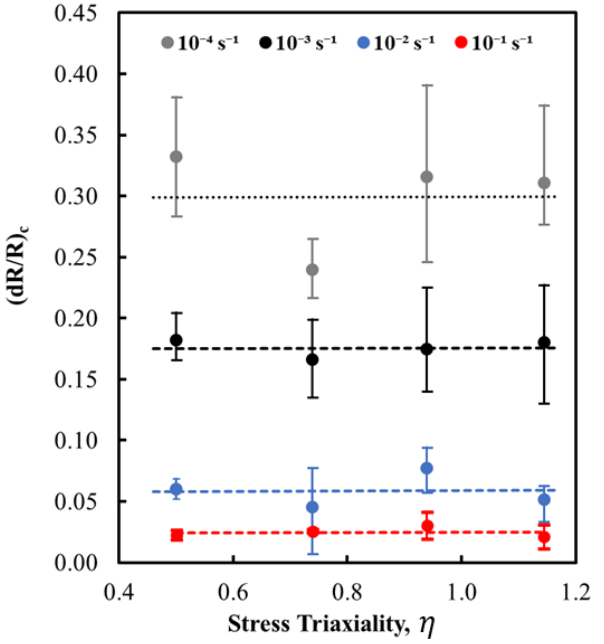

Figure 2.15. Stress independent constant $(dR/R)_c$ as a function of stress triaxiality, η for different strain rates.

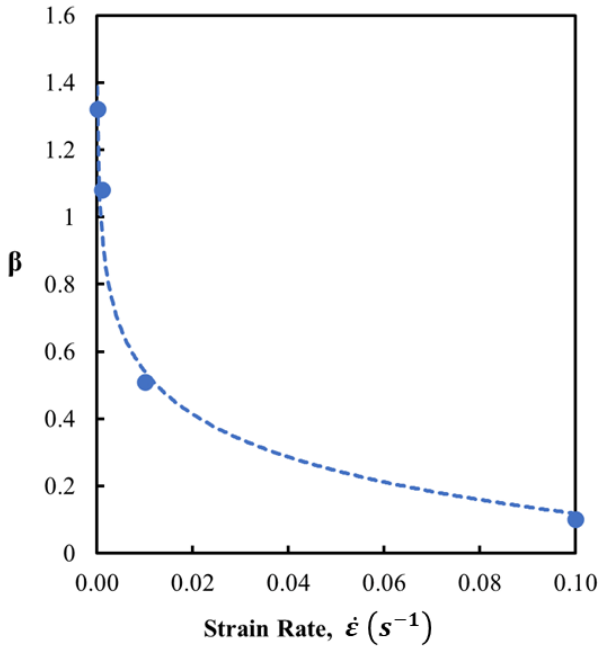

Figure 2.16. β as a function of input strain rate, $\dot{\varepsilon}$.

2.5 Numerical simulations and comparison with experiments

The proposed constitutive theory is implemented as a user material (VUMAT) subroutine in the finite element program ABAQUS/Explicit (ABAQUS 2017). To validate the predictive capabilities of the theory and its numerical implementation, several simulations are carried out on different specimen geometries for the isotactic polypropylene defined in section 2. The response is studied for four separate cases:

(i) A uniaxial tension simulation for a 3D dog-bone geometry (ASTM D638).

(ii) A uniaxial compression simulation of a 3D cylinder.

(iii) Tensile simulation of a thin plate with a circular hole at the center.

(iv) Three-point bending simulation of a notched beam.

For load cases (i) through (iv), the results of the numerical simulations for the macroscopic load-displacement curves are compared against the experimental results for three input strain rates of $10^{-3}\ s^{-1}$, $10^{-2}\ s^{-1}$, and $10^{-1}\ s^{-1}$ respectively.

2.5.1 Uniaxial tension simulation for a 3D dog-bone geometry

For the specimen geometry, a standard tensile dog-bone specimen is used as defined in ASTM D638. For the finite element approach, a 1/8 model as shown in Fig. 2.17(a) is used. Symmetry conditions are used along the symmetry planes as shown and a time dependent displacement of 20 mm is applied to the top surface of the sample. The domain is discretized as shown in Fig. 2.17(b) using 8-noded hexahedron elements (C3D8R) with reduced integration. To regularize the mesh density for the damage simulation, the minimum element size is set to be as 0.36 mm.

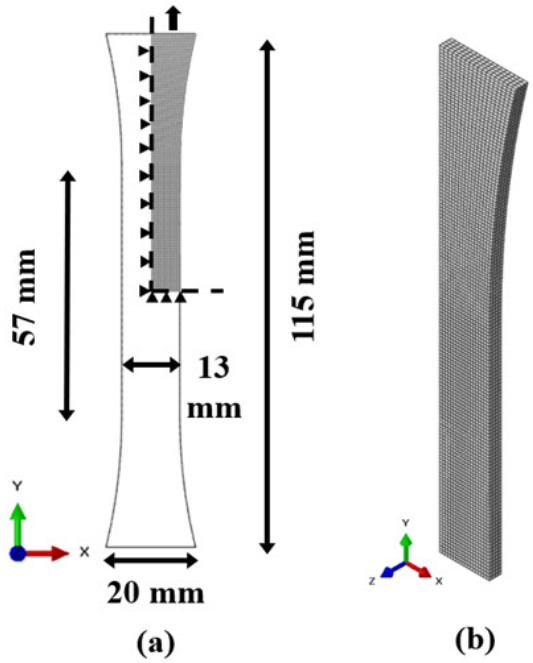

Figure 2.17. (a) Specimen geometry and boundary conditions. (b) 8-noded hexahedron mesh using C3D8R elements.

Fig. 2.18 shows the results from the simulation. It is seen that the model is able to predict the load-deformation response captured through the yield point and ultimate failure point. For the low strain rate of $10^{-3}\ s^{-1}$ in Fig. 2.18(a), the simulation model captures the yield point reasonably well but begins to deviate from the test response when the material starts to draw as shown in Fig. 2.18(a) at load-point (3), due to collapsing of the elements in the FE mesh. For the two higher strain rates of $10^{-2}\ s^{-1}$, and $10^{-1}\ s^{-1}$ respectively, the response is captured well and there is a good agreement with the post yield response until failure. Contour plots of the maximum principal stress σ_1, and the equivalent plastic shear strain ε_{eq}^{p}, corresponding to point (1) in the load-displacement plot, are shown in Fig. 2.18(b) and (c), respectively just prior to critical fracture for the strain rate of $10^{-1}\ s^{-1}$.

Both contours indicate that cavitation induced damage initiates in the gage section and continues to evolve along the cross section until the state of complete fracture.

Fig. 2.18(d) shows the resulting damage variable, d at full fracture where the elements are removed for $d \approx d_c$ to show the damage propagation. For the low strain rate of $10^{-3}\ s^{-1}$, the maximum principal strain contour plot is shown in Fig. 2.18(e) as the sample exhibits plasticity, necking, and a significant drawing at location (3) beyond which the finite elements begin to collapse due to excessive deformation. As can be seen from Fig. 2.18(e), the post-yield softening response is under predicted by the model for $10^{-3}\ s^{-1}$ as the specimen begins to neck. This might be due to the model's inability to capture the micro mechanisms involved during the chain realignment phase in the post-yielding regime causing significant necking.

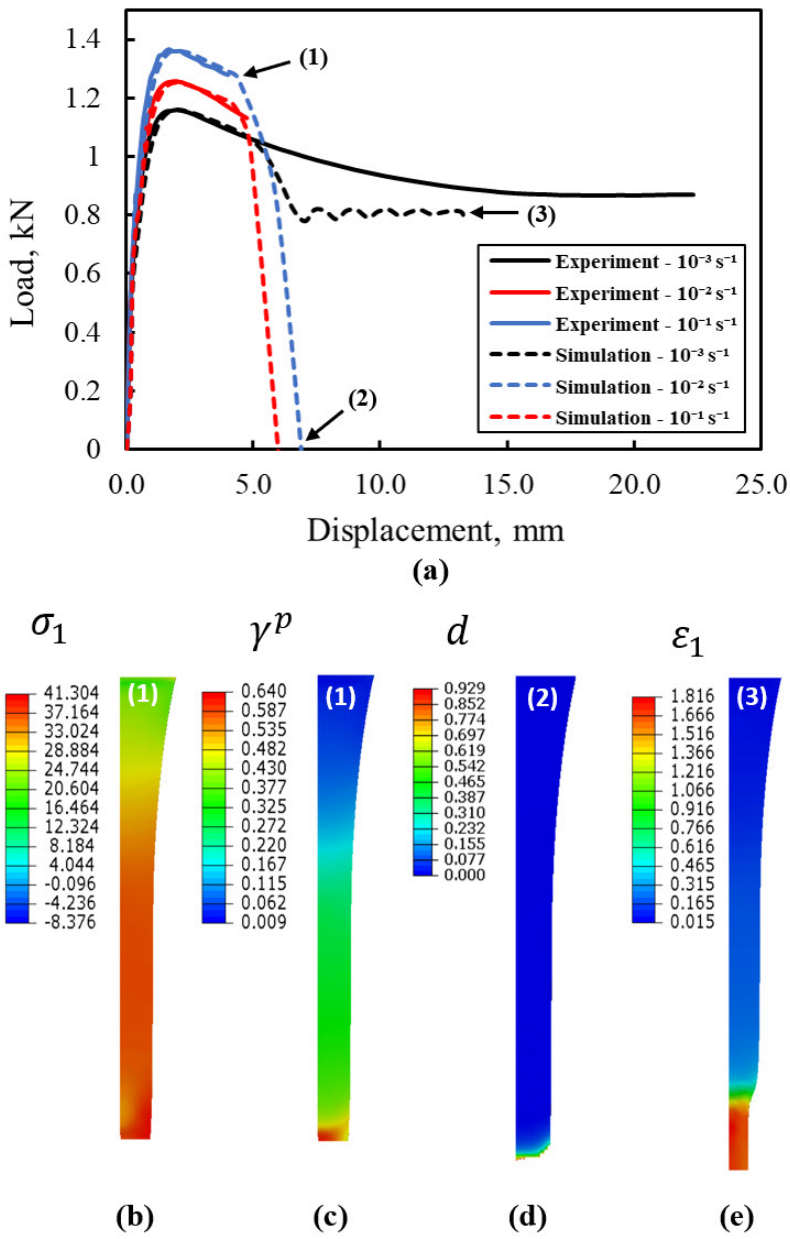

Figure 2.18. (a) Comparison between the model prediction and experimental load-displacement curve. (b) Maximum principal stress contour corresponding to load point (1). (c) Equivalent plastic shear strain contour corresponding to load point (1). (d) Damage variable, d, corresponding to point (2) right after complete fracture. (e) Principal logarithmic strain at point (3) as the neck propagates for the $10^{-3}\ s^{-1}$ strain rate along the gauge section.

2.5.2 Uniaxial compression simulation of a 3D cylinder

The specimen geometry used for this study is shown in Fig. 2.19(a). The three-dimensional geometry is modeled considering 1/4 symmetry, using ABAQUS 8-noded hexahedron (C3D8R) elements with reduced integration as shown in Fig. 19(b). Two rigid platens are used to compress the 1/4 cylinder and a frictional constant of 0.05 is defined between the sample and the platens to avoid slippage at the grip. A time dependent displacement of 5 mm is applied to the top platen and the model prediction from the simulation is plotted in Fig. 2.20.

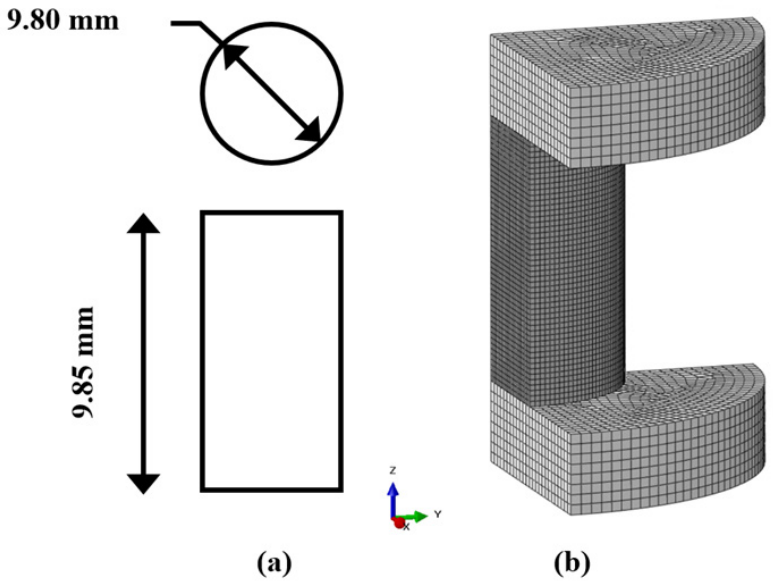

Figure 2.19. (a) Experimental specimen geometry. (b) 1/4 model finite element mesh discretization using ABAQUS-C3D8R elements.

Fig. 2.20(a) shows the rate dependent load-displacement response in comparison to the experimental results for three different strain rates. As shown, the model is able to predict the rate dependent, large deformation response reasonably well. Contour plots of the maximum principal stress σ_1, and the equivalent plastic shear strain rate γ^p, corresponding to point (1) in the load-deformation curve are shown in Fig. 2.20(b) and (c), respectively just prior to element collapse for the strain rate of $10^{-1}\ s^{-1}$. Similar to the experimental results, the simulations show the barreling effect and the corresponding tensile stress field created due to the transverse shear in Fig. 2.20(b). Fig. 2.20(d) shows the contour plot of the maximum principal strain just prior to the element collapse at an engineering strain of 0.5 mm/mm corresponding to location (1).

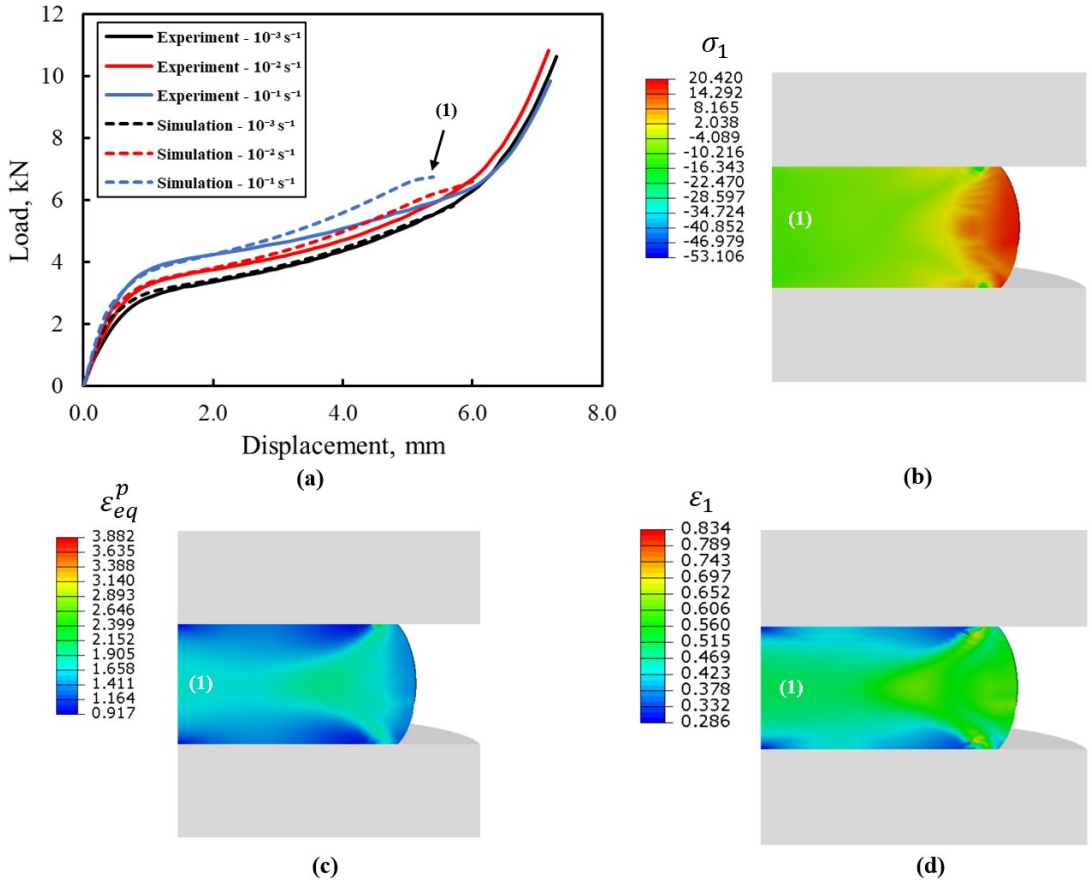

Figure 2.20. (a) Comparison between the experiments and numerically predicted load-displacement curve. (b) Maximum principal stress plot corresponding to load point (1). (c) Equivalent plastic shear strain corresponding to load point (1). (d) Maximum principal logarithmic strain corresponding to load point (1).

2.5.3 Tensile simulation of a thin plate with circular hole at the center

The specimen geometry used for this simulation is shown in Fig. 2.21(a). The three-dimensional geometry is modeled considering 1/4 symmetry, with the help of 8-noded hexahedron elements (C3D8R) in ABAQUS with reduced integration as shown in Fig. 2.21(b). The top surface is displaced 10 mm in the vertical direction. To regularize the mesh density, the minimum element size is considered as 0.23 mm in the localized plastic strain region.

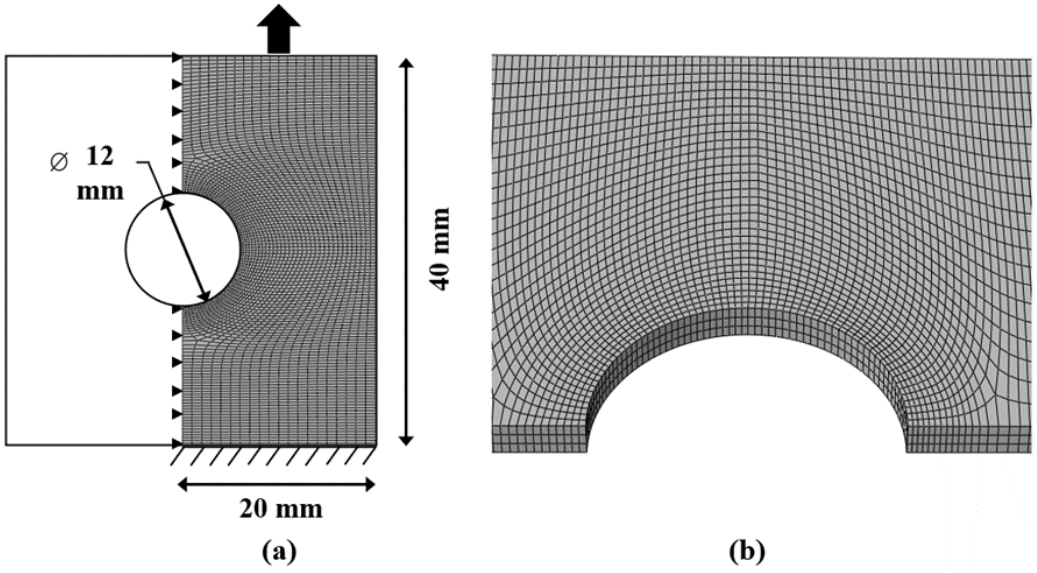

Figure 2.21. (a) Specimen geometry for the plate with a hole simulation. (b) Finite element mesh discretization using ABAQUS-C3D8R elements.

Fig. 2.22(a) shows the corresponding model predicted force-displacement curves as compared with the experimental results. For the low strain rate, the sample behaves similar as the tensile bar and continues to draw to a large stretch ratio. The simulation results capture the yield point well for the $10^{-3}\ s^{-1}$ and the $10^{-1}\ s^{-1}$ strain rates, respectively. The model prediction corresponding to the input strain rate of $10^{-2}\ s^{-1}$ matches the stiffness well, yet the damage response is relatively softer compared to the experimental result. Contour plots of the maximum principal stress σ_1, and the equivalent plastic shear strain corresponding to point (1) in the load-displacement curve are shown in Fig. 2.22(b) and (c), respectively just prior to the complete failure for the strain rate of $10^{-1}\ s^{-1}$. Both contours indicate that cavitation induced damage initiates in the gage section and evolves along the cross section until complete fracture has occurred. Fig. 2.22(d) shows the contour of the resulting damage variable, d with the elements being removed for $d \approx d_c$ to show complete fracture. An image of the cracked sample is also provided to compare with the experimental crack path as shown in Fig. 2.22(e). Further, in Fig. 2.22(f) and (g) a good agreement has been observed between the model predicted maximum principal strain, ε_1 and the experimental Digital Image Correlation result for the strain contour ε_{22}.

Similar to the dogbone specimen, the post-yield softening response is under predicted for $10^{-3}\ s^{-1}$, as the sample begins to neck and the molecular chains arrange themselves into the aligned state. Likewise, the discrepancy between the experiment and model prediction in this lower strain rate regime is arising due to the model's inability to capture the micro mechanism involved in the chain realignment phase.

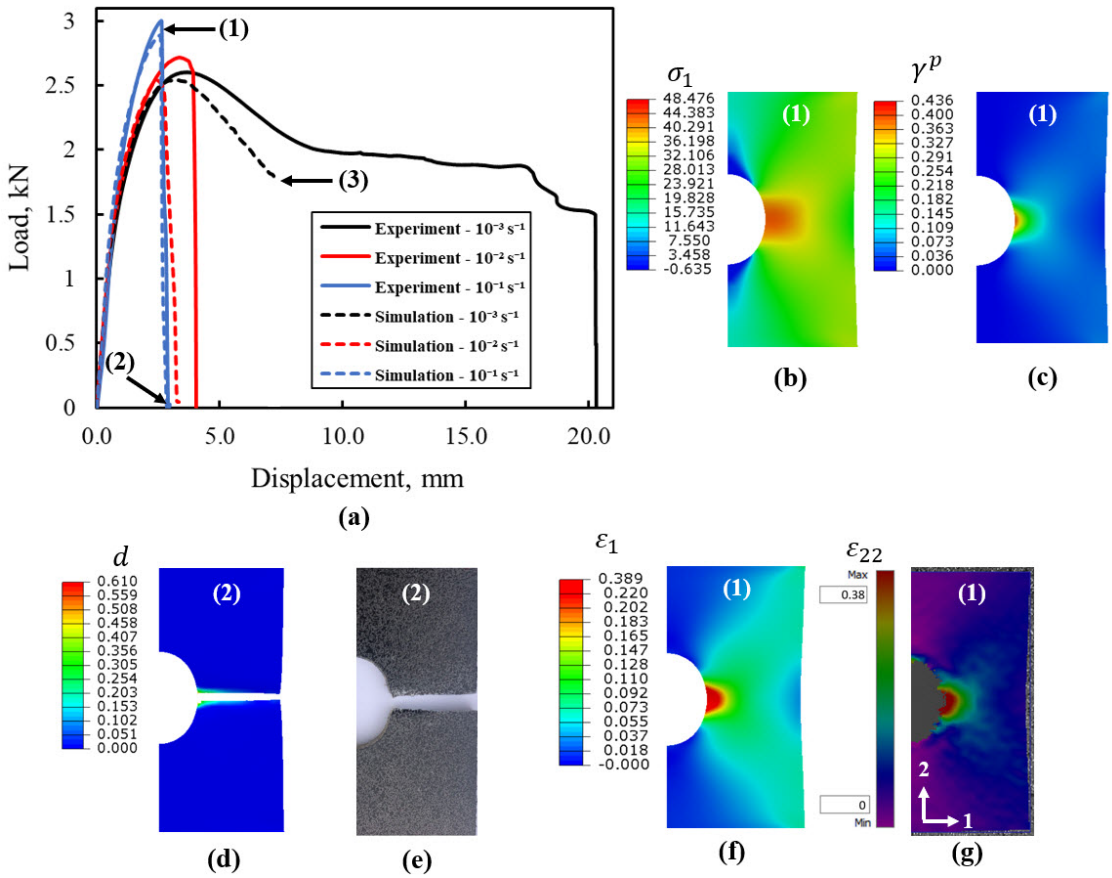

Figure 2.22. (a) Comparison between the experiments and model predicted load-displacement curves at different strain rates. (b) Maximum principal stress plot corresponding to load point (1). (c) Equivalent plastic shear strain corresponding to load point (1). (d) Damage variable, d, corresponding to point (2) right after complete fracture (model prediction). (e) Cracked specimen, showing the physical crack path in the experiment. (f) Maximum principal strain ε_1 corresponding to point (1). (g) Experimental DIC strain contour for (ε_{22}).

2.5.4 Three-point bending of a notched beam

The geometry and the boundary conditions for the three-point bending beam simulation are shown in Fig. 2.23(a).

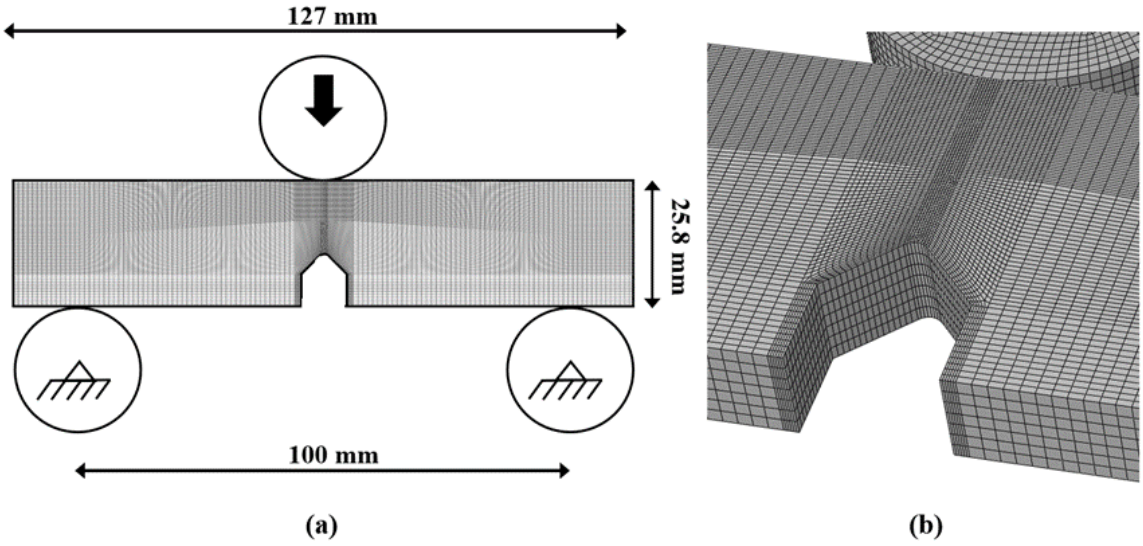

Figure 2.23. (a) Simulation specimen for the three-point bend geometry. (b) Finite element mesh discretization using ABAQUS-C3D8R elements.

The beam has a notch of 1.5mm in length and 1.2mm tip diameter at the mid-span. The three-dimensional geometry is modeled considering 1/2 symmetry, using 8-noded hexahedron (C3D8R) ABAQUS elements with reduced integration. Fig. 2.23(b) shows

the representative mesh discretization. The model is displaced for 15 mm in the vertical direction and a friction coefficient of 0.1 is used to resist the slippage between the 25.4 mm diameter rollers and the beam. The rollers are modeled as rigid elements. To regularize the mesh density in the plastic zone, the minimum element size is chosen as 0.22 mm for this simulation.

Fig. 2.24(a) shows the experimental and model predicted load-displacement curves for the notched beam. The yield point of the load-displacement curve and damage response is captured reasonably well by the model for the higher strain rates of $10^{-2}\ s^{-1}$ and $10^{-1}\ s^{-1}$. For the low strain rate of $10^{-3}\ s^{-1}$ the experimental result shows a damage response, which is not captured by the simulation as the damage model is considered to be inactive in the lower strain rate regime. It is to note that the experimental notched beam samples were designed to have thickness such that a plane strain situation prevails promoting fracture; whereas based on the transition strain rate of $10^{-3}\ s^{-1}$ in the modeling only shear yielding mechanism is considered. Hence, the simulation does not show any damage response. The transition rate of $10^{-3}\ s^{-1}$, below which the damage model is considered inactive has been chosen based on the tensile stress-strain data and may not be accurate for multiaxial stress-state in plane strain dominated geometries. Hence, further exploration is required in future study.

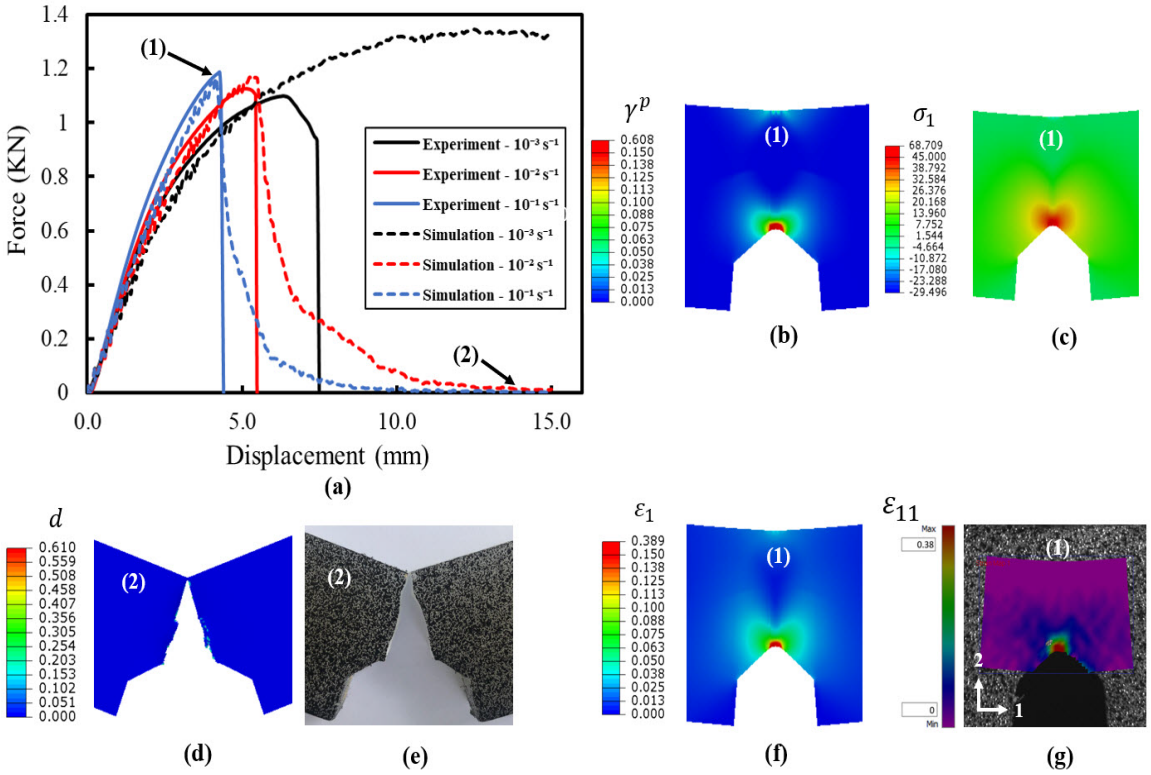

Figure 2.24. Comparison between the experiments and numerically predicted load-displacement curve. (b) Maximum principal stress plot corresponding to load point (1). (c) Equivalent plastic shear strain corresponding to load point (1). (d) Damage variable, *d*, corresponding to point (2) right after complete fracture (simulation). (e) Cracked specimen, showing the physical crack path in the experiment. (f) Maximum principal strain ε_1 corresponding to point (1). (g) Experimental DIC strain contour for (ε_{22}).

In addition to the load-deformation plot, the contour plots of the maximum principal stress σ_1, and the equivalent plastic shear strain ε_{eq}^{p}, corresponding to point (1) in the load-displacement curve are shown in Fig. 2.24(b) and 2.24(c), respectively just prior to final fracture for the strain rate of $10^{-1}\ s^{-1}$. Both contours show the evolution of the plastic

strain field and cavitation induced damage initiation around the notch tip and its propagation until complete fracture has happened. Fig. 2.24(d) shows the resulting damage variable, d just prior to complete fracture. Further, Fig. 2.24(f) and (g) show a good correlation between the model predicted maximum principal strain, ε_1 and the experimentally obtained Digital Image Correlation result for ε_{11} .

.

2.6 Concluding remarks

In this work, a large deformation elastic-viscoplastic constitutive model coupled with a continuum damage mechanics approach is presented for predicting rate-dependent failure response of the semicrystalline polymers. The constitutive theory is based on a rate-dependent viscoplastic flow rule to characterize the yield dominated response in semicrystalline polymers. The occurrence of cavitation growth, coalescence, and fibrillation is modeled with a continuum scale damage evolution, where the strain rate dependence and the stress triaxiality are considered as influencing parameters. Further, a cut-off strain rate of 10^{-3} s^{-1} is considered below which the damage model is not active in favor of a shear yielding mechanism. Hence the proposed unified framework, can predict both the shear yielding and cavitation induced damage phenomena in the materials based on the input strain rate. The proposed model is implemented into a commercial finite-element program and various simulations are conducted. It is seen that, with the material

parameters properly calibrated, the model is able to reasonably-well predict the macroscopic load-displacement curves, local aspects of plasticity, and damage growth until final fracture.

3 Future recommendations

The following items are recommended as future tasks:

- A limitation of the present model shows that the existing shear-yield model underpredicts the stiffness response during the drawing phase of the material. Future exploration of the micromechanics parameters should be explored as they develop.

- For the plane-strain beam in three-point bending, fracture is not predicted as the model is not active below the threshold strain rate. Future work should include a deeper understanding of the micromechanics parameters involved with respect to the precise threshold strain between shear-yield damage and cavitation damage. Additionally, the present study considered uniaxial test data only to calibrate the damage model whereas future models should consider multiaxial stress states

- A limitation of the proposed methodology is that many semicrystalline polymers have degradation mechanisms that involve crazing, cavitation, combinations of

the two, or neither of the two at all. Although the constitutive model may certainly still have very good correlation with the macromolecular response for non-cavitating semicrystalline polymers, the primary drawback of the presented damage model is the focus on only cavitation growth and coalescence. Future work could couple the existing constitutive equations with known damage response for the semicrystalline polymer of interest.

- In the present study, the flow rule is limited to isothermal processes only. This work only considers the rate dependent, large strain constitutive response for isotactic polypropylene homopolymer at room temperature. This work does not consider the direct thermal heating due to molecular friction during rate dependent loads, however this proposed methodology can be extended further to included other applied isothermal temperatures above the glass transition temperature.

- The coupled viscoplastic-damage model could also be extended to model other semicrystalline polymers that are know to exhibit similar marco level responses

with cavitation damage mechanisms, such as polyoxymethylene (POM) and high density polyethylene (HDPE).

4 References

1. Abaqus/Explicit, 2017. Abaqus inc. Providence, Rhode Island, United States.

2. Ames, Nicoli M., et al. "A thermo-mechanically coupled theory for large deformations of amorphous polymers. Part II: Applications." *International Journal of Plasticity* 25.8 (2009): 1495-1539.

3. Anand, L., and N. M. Ames. "On modeling the micro-indentation response of an amorphous polymer." *International journal of plasticity* 22.6 (2006): 1123-1170.

4. Anand, Lallit, and Morton E. Gurtin. "A theory of amorphous solids undergoing large deformations, with application to polymeric glasses." *International Journal of Solids and Structures* 40.6 (2003): 1465-1487.

5. Anand, Lallit, et al. "A thermo-mechanically coupled theory for large deformations of amorphous polymers. Part I: Formulation." *International Journal of Plasticity* 25.8 (2009): 1474-1494.

6. Argon, A. S. "A theory for the low-temperature plastic deformation of glassy polymers." *Philosophical Magazine* 28.4 (1973): 839-865.

7. Arruda, Ellen M., Mary C. Boyce, and R. Jayachandran. "Effects of strain rate, temperature and thermomechanical coupling on the finite strain deformation of glassy polymers." *Mechanics of Materials* 19.2-3 (1995): 193-212.

8. Ayoub, Georges, et al. "Modelling large deformation behaviour under loading–unloading of semicrystalline polymers: application to a high density polyethylene." *International Journal of Plasticity* 26.3 (2010): 329-347.

9. Balieu, Romain, et al. "A fully coupled elastoviscoplastic damage model at finite strains for mineral filled semi-crystalline polymer." International Journal of plasticity 51 (2013): 241-270

10. Barba, D., A. Arias, and D. Garcia-Gonzalez. "Temperature and strain rate dependences on hardening and softening behaviours in semi-crystalline polymers: Application to PEEK." International Journal of Solids and Structures 182 (2020): 205-217.

11. Boyce, Mary Cunningham. *Large inelastic deformation of glassy polymers*. Diss. Massachusetts Institute of Technology, 1986.

12. Cayzac, Henri-Alexandre, Kacem Saï, and Lucien Laiarinandrasana. "Damage based constitutive relationships in semi-crystalline polymer by using multi-mechanisms model." International Journal of Plasticity 51 (2013): 47-64.

13. Chaboche, Jean-Louis. "Continuum damage mechanics: Part II—Damage growth, crack initiation, and crack growth." (1988): 65-72.

14. Chen, Ran, et al. "Two-step cavitation in semi-crystalline polymer during stretching at temperature below glass transition." Journal of Polymer Science Part B: Polymer Physics 54.19 (2016): 2007-2014.

15. Detrez, Fabrice, Sabine Cantournet, and Roland Seguela. "Plasticity/damage coupling in semi-crystalline polymers prior to yielding: Micromechanisms and damage law identification." Polymer 52.9 (2011): 1998-2008.

16. Drozdov, A. D., and A. L. Kalamkarov. "A constitutive model for nonlinear viscoelastic behavior of polymers." Polymer Engineering & Science 36.14 (1996): 1907-1919.

17. Drozdov, Aleksey D., and J. deC. Christiansen. "Constitutive equations for the viscoplastic response of isotactic polypropylene in cyclic tests: The effect of strain rate." Polymer Engineering & Science 44.3 (2004): 548-556.

18. Drozdov, Aleksey D., and Jesper deClaville Christiansen. "Model for the viscoelastic and viscoplastic responses of semicrystalline polymers." Journal of applied polymer science 88.6 (2003): 1438-1450.

19. Drozdov, Aleksey D., and Qiang Yuan. "Effect of annealing on the viscoelastic and viscoplastic responses of low-density polyethylene." Journal of Polymer Science Part B: Polymer Physics 41.14 (2003): 1638-1655.

20. Drozdov, Aleksey D., and Qiang Yuan. "The viscoelastic and viscoplastic behavior of low-density polyethylene." *International journal of solids and structures* 40.10 (2003): 2321-2342.

21. Eyring, Henry. "Viscosity, plasticity, and diffusion as examples of absolute reaction rates." *The Journal of chemical physics* 4.4 (1936): 283-291.

22. Francis, D. K., et al. "Formulation of a damage internal state variable model for amorphous glassy polymers." International Journal of Solids and Structures 51.15-16 (2014): 2765-2776.

23. Gurson, Arthur L. "Continuum theory of ductile rupture by void nucleation and growth: Part I—Yield criteria and flow rules for porous ductile media." (1977): 2-15.

24. Gurtin, Morton E., Eliot Fried, and Lallit Anand. *The mechanics and thermodynamics of continua*. Cambridge University Press, 2010.

25. Hassan, Tasnim, Ozgen U. Çolak, and Patricia M. Clayton. "Uniaxial strain and stress-controlled cyclic responses of ultrahigh molecular weight polyethylene: experiments and model simulations." *Journal of engineering materials and technology* 133.2 (2011).

26. Haward, R. N., and G. 1. Thackray. "The use of a mathematical model to describe isothermal stress-strain curves in glassy thermoplastics." *Proceedings of the Royal Society of London. Series A. Mathematical and Physical Sciences* 302.1471 (1968): 453-472.

27. Holmes, D. W., J. G. Loughran, and H. Suehrcke. "Constitutive model for large strain deformation of semicrystalline polymers." Mechanics of Time-Dependent Materials 10.4 (2006): 281-313.

28. Hughes, Thomas JR. "Numerical implementation of constitutive models: rate-independent deviatoric plasticity." *Theoretical foundation for large-scale computations for nonlinear material behavior*. Springer, Dordrecht, 1984. 29-63.

29. Jabbari-Farouji, Sara, et al. "Plastic deformation mechanisms of semicrystalline and amorphous polymers." ACS Macro Letters 4.2 (2015): 147-150.

30. Khaleghi, Hassan, Ahmad Amiri-Rad, and Mohammad Mashayekhi. "A thermodynamically consistent continuum damage model for time-dependent failure of thermoplastic polymers." International Journal of Plasticity 154 (2022): 103278.

31. Kontou, E., and P. Farasoglou. "Determination of the true stress–strain behaviour of polypropylene." *Journal of materials science* 33.1 (1998): 147-153.

32. Krairi, Anouar, and Issam Doghri. "A thermodynamically-based constitutive model for thermoplastic polymers coupling viscoelasticity, viscoplasticity and ductile damage." International Journal of Plasticity 60 (2014): 163-181.

33. Krempl, Erhard, and Kwangsoo Ho. "An overstress model for solid polymer deformation behavior applied to Nylon 66." *Time dependent and nonlinear effects in polymers and composites*. ASTM International, 2000.

34. Laiarinandrasana, Lucien, et al. "Temperature dependent mechanical behaviour of PVDF: experiments and numerical modelling." International Journal of Plasticity 25.7 (2009): 1301-1324.

35. Lemaitre, Jean. "Coupled elasto-plasticity and damage constitutive equations." Computer methods in applied mechanics and engineering 51.1-3 (1985): 31-49.

36. Lu, Ying, and Yongfeng Men. "Cavitation-Induced Stress Whitening in Semi-Crystalline Polymers." Macromolecular Materials and Engineering 303.11 (2018): 1800203.

37. Mulliken, A. D., and M. C. Boyce. "Mechanics of the rate-dependent elastic–plastic deformation of glassy polymers from low to high strain rates." *International journal of solids and structures* 43.5 (2006): 1331-1356.

38. Narayan, Sooraj, and Lallit Anand. "Fracture of amorphous polymers: A gradient-damage theory." Journal of the Mechanics and Physics of Solids 146 (2021): 104164.

39. Nguyen, V-D., et al. "A large strain hyperelastic viscoelastic-viscoplastic-damage constitutive model based on a multi-mechanism non-local damage continuum for amorphous glassy polymers." International Journal of Solids and Structures 96 (2016): 192-216.

40. Pawlak, Andrzej, and Andrzej Galeski. "Plastic deformation of crystalline polymers: the role of cavitation and crystal plasticity." Macromolecules 38.23 (2005): 9688-9697.

41. Pawlak, Andrzej, Andrzej Galeski, and Artur Rozanski. "Cavitation during deformation of semicrystalline polymers." Progress in polymer science 39.5 (2014): 921-958.

42. Pawlak, Andrzej. "Cavitation during tensile deformation of isothermally crystallized polypropylene and high-density polyethylene." Colloid and polymer science 291.4 (2013): 773-787.

43. Peric, D., and D. R. J. Owen. "Finite-element applications to the nonlinear mechanics of solids." Reports on Progress in Physics 61.11 (1998): 1495.

44. Popelar, C. F., C. H. Popelar, and V. H. Kenner. "Viscoelastic material characterization and modeling for polyethylene." *Polymer Engineering & Science* 30.10 (1990): 577-586.

45. Pouriayevali, H., et al. "A constitutive description of the rate-sensitive response of semi-crystalline polymers." International Journal of Impact Engineering 62 (2013): 35-47.

46. Praud, Francis, et al. "Phenomenological multi-mechanisms constitutive modelling for thermoplastic polymers, implicit implementation and experimental validation." Mechanics of Materials 114 (2017): 9-29.

47. Rice, J. R_, and Dennis Michael Tracey. "On the ductile enlargement of voids in triaxial stress fields∗." *Journal of the Mechanics and Physics of Solids* 17.3 (1969): 201-217.

48. Richeton, J., et al. "Influence of temperature and strain rate on the mechanical behavior of three amorphous polymers: Characterization and modeling of the compressive yield stress." International journal of solids and structures 43.7-8 (2006): 2318-2335.

49. Robertson, Richard E. "Theory for the plasticity of glassy polymers." *The Journal of Chemical Physics* 44.10 (1966): 3950-3956.

50. Schapery, Richard A. "Correspondence principles and a generalized J integral for large deformation and fracture analysis of viscoelastic media." *International journal of fracture* 25.3 (1984): 195-223.

51. Shen, Fei, et al. "Thermo-elastic-viscoplastic-damage model for self-heating and mechanical behavior of thermoplastic polymers." International Journal of Plasticity 121 (2019): 227-243.

52. Srivastava, Vikas, et al. "A thermo-mechanically-coupled large-deformation theory for amorphous polymers in a temperature range which spans their glass transition." *International Journal of Plasticity* 26.8 (2010): 1138-1182.

53. Tvergaard, Viggo. "On localization in ductile materials containing spherical voids." International Journal of fracture 18.4 (1982): 237-252

54. Voyiadjis, George Z., Amir Shojaei, and Guoqiang Li. "A generalized coupled viscoplastic–viscodamage–viscohealing theory for glassy polymers." International Journal of Plasticity 28.1 (2012): 21-45.

55. Voyiadjis, George Z., Amir Shojaei, and Guoqiang Li. "A thermodynamic consistent damage and healing model for self healing materials." International Journal of Plasticity 27.7 (2011): 1025-1044.

56. Wang, J., et al. "A finite strain thermodynamically-based constitutive modeling and analysis of viscoelastic-viscoplastic deformation behavior of glassy polymers." International Journal of Plasticity 122 (2019): 135-163.

57. Wang, Jun, et al. "A damage-based elastic-viscoplastic constitutive model for amorphous glassy polycarbonate polymers." Materials & Design 97 (2016): 519-531.

58. Wang, Tie Jun, Kikuo Kishimoto, and Mitsuo Notomi. "A micromechanics criterion for the ductile fracture of a polycarbonate." *Key Engineering Materials*. Vol. 183. Trans Tech Publications Ltd, 2000.

59. Wang, Tie-Jun. "Improved local void growth ratio criterio for ductile fracture." *International journal of fracture* 57.1 (1992): R3-R6.

60. Wu, P. D., and Erik van der Giessen. "On neck propagation in amorphous glassy polymers under plane strain tension." *International Journal of Plasticity* 11.3 (1995): 211-235.

61. Zaïri, Fahmi, et al. "A physically-based constitutive model for anisotropic damage in rubber-toughened glassy polymers during finite deformation." International Journal of Plasticity 27.1 (2011): 25-51.

62. Zaïri, Fahmi, et al. "Modelling of the elasto-viscoplastic damage behaviour of glassy polymers." International Journal of Plasticity 24.6 (2008): 945-965.

63. Zhang, Yi, et al. "Quantification of strain-induced damage in semi-crystalline polymers: a review." Journal of Materials Science 54.1 (2019): 62-82.

64. Zienkiewicz, O. C., and R. L. Taylor. "The Finite Element Method, Volume 2: Solid and Fluid Mechanics." Dynamics and Non-Linearity (1991): 1503-1513.

Appendix

A.1 Numerical implementation of the explicit stress update

In this section, the numerical implementation of the constitutive theory outlined in chapter 2 is presented as a simple forward-Euler algorithm and shown below. This is used along with the well-known central difference method [64].

- Known at time t_n: $\boldsymbol{F}_n$, $\boldsymbol{F}^p_n$, $\dot{\gamma^p}_n$, $\boldsymbol{S}^e_n$, $\boldsymbol{S}^e_{0_n}$, S_{1_n}, ϕ_n
- Given at time t_{n+1}: $\boldsymbol{F}_{n+1}$

Step 1: Back-stress, $\boldsymbol{S_{back}}$ at time = t_n

Using the explicit forward Euler approach, the pressure and mean normal stress at time, t_n is calculated as,

$$\bar{p}_n = -\frac{1}{3}(tr\, \boldsymbol{S}^e{}_n)\boldsymbol{I} \quad \text{and} \quad \sigma_{m_n} = -\bar{p}_n \tag{A1}$$

Following which, the plastic component of the left Cauchy-Green tensor is defined as,

$$\boldsymbol{B}^{p}{}_{n} = \boldsymbol{F}^{p}{}_{n}\boldsymbol{F}^{p^{T}}{}_{n} \tag{A2}$$

where the deviatoric component of the left Cauchy-Green tensor is then determined as,

$$\boldsymbol{B}^{p}_{0}{}_{n} = -\frac{1}{3}(tr\ \boldsymbol{B}^{p}{}_{n})\boldsymbol{I} \tag{A3}$$

The effective distortional plastic stress is defined as,

$$\lambda^{p}{}_{n} = \frac{1}{\sqrt{3}}\sqrt{tr(\boldsymbol{B}^{p}{}_{n})} \tag{A4}$$

and back stress modulus μ at time t_n is then calculated as,

$$\mu_n = \mu_R \frac{\lambda_L}{3\lambda^{p}{}_{n}} \frac{\lambda^{p}{}_{n}}{\lambda_L} \left(\frac{3 - \left(\frac{\lambda^{p}{}_{n}}{\lambda_L}\right)^2}{1 - \left(\frac{\lambda^{p}{}_{n}}{\lambda_L}\right)^2} \right) \tag{A5}$$

In cases where the mean normal stress is positive (tension), then μ_n will be stored as a tensile value (as λ_L is a tensile material parameter). Likewise, when the value of the mean normal stress is negative (compression), then μ_n will be stored as a compressive value (as λ_L is a compressive material parameter).

Finally, the back stress equation (Eq. 2.16) taken at time = t_n, for either tension or compression at the material point is calculated as,

$$\boldsymbol{S}_{\boldsymbol{back}_n} = \mu_n \boldsymbol{B}^p_{0_n} \tag{A6}$$

Step 2: Direction of plastic flow, $\boldsymbol{N}_p$ at time = t_n

New notation is introduced here to capture the direction of plastic flow, defined in Eq. 2.20 as for either tension or compression as,

$$\boldsymbol{N}_p = \frac{(\boldsymbol{S}^e_0)_{eff}}{2\bar{\tau}} = \frac{\boldsymbol{S}^e_0 - \boldsymbol{S}_{back}}{2\bar{\tau}} \tag{A7}$$

Where the deviatoric component of the second Piola-Kirchoff elastic stress is defined at time = t_n as,

$$\boldsymbol{S}^e_{0_n} = -\frac{1}{3}(tr\ \boldsymbol{S}^e{}_n)\boldsymbol{I} \tag{A8}$$

and the equivalent shear stress (Eq. 2.22) is defined as,

$$\bar{\tau}_n = \frac{1}{\sqrt{2}} \left| \boldsymbol{S}^e_{0_n} - \boldsymbol{S}_{\boldsymbol{back}_n} \right| \tag{A9}$$

and the direction of plastic flow, $\boldsymbol{N}_{p_n}$ for either tension or compression at the material point is then calculated as,

$$\boldsymbol{N}_{p_n} = \frac{\boldsymbol{S}^e_{0_n} - \boldsymbol{S}_{\boldsymbol{back}_n}}{2\bar{\tau}_n} \tag{A10}$$

Step 3: Stress triaxiality ratio, η at time = t_n

The mean normal stress is defined in Eq. A1. The von Mises equivalent stress is defined as,

$$\sigma_{eq_n} = \sqrt{\frac{3}{2} \boldsymbol{S}^e_{0_n} : \boldsymbol{S}^e_{0_n}} \tag{A12}$$

leading to the definition of triaxiality at time = t_n as,

$$\eta_n = \frac{\sigma_{m_n}}{\sigma_{eq_n}} \tag{A13}$$

Step 4: Plastic flow rule, $\boldsymbol{F}^{P}{}_{n}$ at time = t_{n+1}

Using the forward Euler approach at time = t_{n+1}, the flow rule is now able to be calculated from our first step at time = t_n. The net shear stress for thermally activated flow as shown in Eq. 2.24 is now calculated as,

$$\tau_{e_n} \stackrel{\text{def}}{=} \bar{\tau}_n - \left(S_{1_n} + \alpha_p \bar{p}_n\right) \tag{A14}$$

This now leads to the first forward time step for the calculation of the equivalent plastic shear strain rate taken from Eq. 2.23 as:

$$\dot{\gamma^p}_{n+1} = \dot{\gamma}_0 exp\left\{\frac{Q}{-k_B\vartheta}\right\}\left[sinh\left(\frac{\tau_{e_n}V}{2k_B\vartheta}\right)\right]^{\frac{1}{m}} \tag{A15}$$

where $\dot{\gamma^p}_{n+1}$ can again take on a tensile or compressive value at the material point depending on the sign of the mean normal stress. The plastic flow rule is taken from Eq. 2.19 and then integrated to give the plastic deformation gradient for tension or compression as,

$$\boldsymbol{F}_{n+1}^{p} = \boldsymbol{F}_{n}^{p} + \dot{\gamma}^{p}{}_{n+1}\boldsymbol{F}_{n}^{p} \tag{A16}$$

Step 5: Cauchy stress, $\boldsymbol{T}^{e}$ at time = t_{n+1}

Following the logic of the numerical implementation, all calculations below will have either a tensile or compressive value at the material point depending on the sign of the mean normal stress. Now that $\boldsymbol{F}_{n+1}^{p}$ is determined from the last step, $\boldsymbol{F}_{n+1}^{e}$ is now calculated as,

$$\boldsymbol{F}_{n+1}^{e} = \boldsymbol{F}_{n+1}\boldsymbol{F}_{n}^{p^{-1}} \tag{A17}$$

Using $\boldsymbol{F}_{n+1}^{e}$, one can obtain the elastic right Cauchy-Green tensor as,

$$\boldsymbol{C}_{n+1}^{e} = \boldsymbol{F}_{n+1}^{e}{}^{T}\boldsymbol{F}_{n+1}^{e} \tag{A18}$$

Further, the elastic Green strain is then calculated as,

$$\boldsymbol{E}_{n+1}^{e} = \frac{1}{2}(\boldsymbol{C}_{n+1}^{e} - I) \tag{A19}$$

with the deviatoric portion of the Greens strain defined as,

$$\boldsymbol{E}^{e}_{0_{n+1}} = \boldsymbol{E}^{e}{}_{n+1} - \frac{1}{3}(tr\,\boldsymbol{E}^{e}{}_{n+1})\boldsymbol{I} \tag{A20}$$

The second Piola-Kirchoff stress is then updated as,

$$\boldsymbol{S}^{e}{}_{n+1} = 2G\boldsymbol{E}^{e}_{0_{n+1}} + K(tr\boldsymbol{E}^{e}_{n+1})\boldsymbol{I} \tag{A21}$$

Finally, leading to the definition of the damaged Cauchy stress as,

$$\boldsymbol{T}^{e}{}_{n+1} = J\boldsymbol{F}^{e}_{n+1}{}^{-1}\boldsymbol{S}^{e}{}_{n+1}\boldsymbol{F}^{e}_{n+1}{}^{-T} \tag{A22}$$

Step 6: Update of the internal plastic variables S_1 and ϕ at time = t_{n+1}

Similarly, the internal plastic variables below with either be tensile or compressive at the material point. The rate form of the order parameter ϕ, is calculated as,

$$\dot{\phi}_{n+1} = g(\phi^{*} - \phi)\dot{\gamma^{p}}_{n+1} \tag{A23}$$

which is then integrated to determine the scalar value of the order parameter ϕ , at time = t_{n+1}, as:

$$\phi_{n+1} = \phi_n + \dot{\phi}_{n+1}\Delta t \tag{A24}$$

For the coupled equation between S_1 and ϕ, the coupled parameter S_1^* at time = t_{n+1} is updated as,

$$S^*_{1\,n+1} = b(\phi^* - \phi_{n+1}) \tag{A25}$$

Similarly, the rate form of the second internal plastic variables, S_1 is calculated as,

$$\dot{S}_{1\,n+1} = h_1\left(S^*_{1\,n+1} - S_1\right)\dot{\gamma}^p{}_{n+1} \tag{A26}$$

and is then integrated to give,

$$S_{1\,n+1} = S_{1\,n} + \dot{S}_{1\,n+1}\Delta t \tag{A27}$$

Step 7: Update of the damage variable d, at time = t_{n+1}

To incorporate the proposed damage model, the update algorithm is modified as shown below. The algorithm outlined above from step 1 to step 6 remains unchanged except for the following computations:

- If the damage criteria for initiation is met (ie. $\varepsilon_{eq}^{p} \geq \varepsilon_{i}^{p}, \quad$ for $\dot{\varepsilon} \geq 10^{-3}\ s^{-1}$) as defined in Eq. 2.39, then the damaged net shear stress for thermally activated flow is determined by,

$$\tau_{e_n}{}^{D} \stackrel{\text{def}}{=} \bar{\tau}_n - \left((1-d)^2 S_{1_n} + \alpha_p \bar{p}_n\right) \tag{A28}$$

- Likewise, the damaged second Piola-Kirchoff stress is then updated as,

$$\boldsymbol{S}^{e\,D}{}_{n+1} = (1-d)^2\left(2G\boldsymbol{E}^{e}_{0_{n+1}} + K(tr\boldsymbol{E}^{e}_{n+1})\boldsymbol{I}\right) \tag{A29}$$

- Finally, the rate dependent damage variable $\dot{d}_{n+1}$, is updated as,

$$\dot{d}_{n+1} = exp(\beta\eta_{n+1})\frac{\dot{\gamma}^{p}{}_{n+1}}{(1-d)^2} \tag{A30}$$

- following which the rate dependent damage variable is then integrated as,

$$d_{n+1} = d_n + \dot{d}_{n+1}\Delta t \tag{A31}$$